Article

Molecular Dynamics Simulation of Complex Reactivity with the Rapid Approach for Proton Transport and Other Reactions (RAPTOR) Software Package

Scott Kaiser, Zhi Yue, Yuxing Peng, Trung Dac Nguyen, Sijia Chen, Da Teng, and Gregory A. Voth*
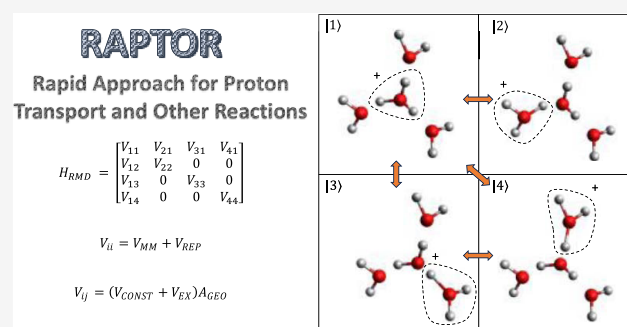
Read Online

ACCESS | 📊 Metrics & More | 📖 Article Recommendations | 🔗 Supporting Information

ABSTRACT: Simulating chemically reactive phenomena such as proton transport on nanosecond to microsecond and beyond time scales is a challenging task. *Ab initio* methods are unable to currently access these time scales routinely, and traditional molecular dynamics methods feature fixed bonding arrangements that cannot account for changes in the system's bonding topology. The Multiscale Reactive Molecular Dynamics (MS-RMD) method, as implemented in the Rapid Approach for Proton Transport and Other Reactions (RAPTOR) software package for the LAMMPS molecular dynamics code, offers a method to routinely sample longer time scale reactive simulation data with statistical precision. RAPTOR may also be interfaced with enhanced sampling methods to drive simulations toward the analysis of reactive rare events, and a number of collective variables (CVs) have been developed to facilitate this. Key advances to this methodology, including GPU acceleration efforts and novel CVs to model water wire formation are reviewed, along with recent applications of the method which demonstrate its versatility and robustness.

$$H_{RMD} = \begin{bmatrix} V_{11} & V_{21} & V_{31} & V_{41} \\ V_{12} & V_{22} & 0 & 0 \\ V_{13} & 0 & V_{33} & 0 \\ V_{14} & 0 & 0 & V_{44} \end{bmatrix}$$

$$V_{ii} = V_{MM} + V_{REP}$$

$$V_{ij} = (V_{CONST} + V_{EX})A_{GEO}$$

1. INTRODUCTION

Molecular dynamics (MD) simulations of chemically reactive phenomena present significant challenges for conventional simulation techniques. On one hand, quantum mechanical methods, such as *ab initio* MD (AIMD) or quantum mechanics/molecular mechanics (QM/MM), that directly compute the electronic structure at each MD time step of a simulation are too expensive to access the time scales needed to describe the dynamics of the larger system.[1−3] On the other hand, standard MD utilizes force fields with a fixed bonding topology[4] that cannot readily account for the dynamic nature of reactive events. QM/MM methods, which compute the electronic structure for only a small portion of reacting atoms and couple that quantum-mechanical region to a larger classical region, have proven valuable for the study of these systems.[5−7] However, they are still generally limited to tens (or at most hundreds) of picosecond time scales for reactive regions on the order of tens to a few hundred atoms, which is often insufficient to capture the full extent of reactivity such as proton shuttling via water "wires" and/or protonatable amino acids in complex systems. Methods incorporating machine learning (ML) approaches, such as neural networks (NNs), in some cases offer results comparable to *ab initio* methods at a fraction of the cost.[8,9] However, these methods face challenges including the need to train on large amounts of *ab initio* data, and they typically do not offer transferability to new chemical spaces. Simulating reactive phenomena on the nanosecond and

microsecond timescales needed to determine, e.g., how protons Grotthuss shuttle[10,11] over long distances, or how protonation behavior impacts protein conformational change, or how proton transport occurs in confined spaces, requires a method that can access longer time and length scales possible than with current *ab initio* methods.[7,12,13]

A promising approach is provided by "multiconfigurational" classical molecular dynamics methods. The first of these to be developed was the empirical valence bond (EVB) model of Warshel and coworkers.[14,15] In the EVB method, one describes a system as a linear combination of "diabatic states", with the possible bonding topologies the system may assume. It is important to note that the "diabatic states" referenced are in fact entirely classical objects, and do not reflect quantum states with their corresponding nonadiabatic dynamics. They are instead more akin to the resonance forms one is familiar with from organic chemistry. Each of these diabatic states is modeled with a force field and a potential is defined to allow for transitions between the states. This "fixed-state" EVB approach, however, is unable to account for the dynamic

transport of excess protons through a hydrogen bonding network, where protons will rapidly "hop" between waters via Grotthuss shuttling.[10,11] To correctly model Grotthuss shuttling, a generalization to Warshel's EVB model was required. This was developed independently, albeit with some differences, by the Voth and Borgis groups in the late 1990s,[16−19] which built upon the earlier work two-state EVB work of Lobaugh and Voth[20] for the hydrated excess proton in water. The resulting model, termed Multistate EVB (MS-EVB), allows for the diabatic states considered in the reaction to evolve dynamically over the course of the simulation, which enables a comprehensive consideration of proton diffusion through a hydrogen bonding network. The Voth group has continued to build upon this model in the following years, improving the numerical stability, accuracy, and computational expense of the approach.[21−28] The most recent variant, MS-EVB 3.2, provides accurate properties for proton transport in bulk water. Various MS-EVB models have also been used to describe the hydrated proton (and proton hole, or hydroxide) in a wider number of environments—most notably describing hydrated excess protons at interfaces,[29−31] as well as proton transport through water "wires" in a number of protein environments[13,32−37] and complex transport in materials such as proton exchange membranes.[38−44]

The MS-EVB approach can, in principle, be also applied to a wide range of chemical reactions. A key advantage is that previously developed classical force fields can be used to describe many of the nonreactive parts of the model, which minimizes the degree of reparameterization necessary.[15,45] The reactive parts of the model are typically fit to *ab initio* electronic structure data on the reaction in question.[26,27,34] The MS-EVB method reflects a paradigm where empirical functional forms are used to describe the Hamiltonian. More recently, the original EVB idea has been generalized as Multiscale Reactive Molecular Dynamics (MS-RMD), which is an expansion of the MS-EVB idea. MS-RMD allows for the potential to be fit not exclusively with potentially limited empirical functional forms, but also with more general, flexible functional forms such as tabulated numerical or neural network-based potentials.[27,46] The MS-RMD method emphasizes that the potentials are fit directly from first-principles chemical data on the reaction in question. In a manner analogous to the construction of a coarse-grained potential at the all-atom scale, fitting a MS-RMD potential involves matching forces (and possibly energies) from higher level QM/MM calculations or single-point QM calculations along the reaction coordinate to fit the coefficients of an empirical force field, or to construct a numerical or neural-network potential that describes the transition between EVB states. The focus of this article will be on the subsequent efficient evaluation of the MS-RMD Hamiltonian and on applications of the MS-RMD approach with the Rapid Approach for Proton Transport and Other Reactions (RAPTOR) MD package. For more information on the fitting of MS-RMD models, the reader is referred to refs. [24,27,34], and [47].

The evaluation of the MS-RMD Hamiltonian involves at each simulation step (1) a "state search" algorithm to determine the EVB bonding topologies (diabatic states) one considers at a given time step, (2) evaluation of the energies and forces for each diabatic state, (3) evaluation of the off-diagonal terms, and 4) diagonalization of the resulting matrix to obtain ground-state forces and energies via the Hellmann−Feynman theorem. Steps (2) and (3) are typically done in

parallel for computational efficiency.[45] A key challenge in computing the energies and forces in the MS-RMD approach is the need to consider a substantial number of EVB states, and to dynamically reconsider or readjust the EVB states that one is evaluating at each time step (for an example, see ref. [23]). This "state search" algorithm must be tuned to consider enough EVB states to ensure, on one hand, the energy conservation and stability of the model; and on the other hand, the model's computational tractability. Increasing the number of EVB states will significantly increase the computational cost—in the naïve implementation, the evaluation of the energies and forces for each diabatic state is the cost of a conventional molecular dynamics (MD) time step. A typical simulation of hydrated excess proton transport in water requires about 20 EVB states to ensure accuracy and energy conservation.[23] As a result of the high number of EVB states required in the MS-RMD approach, techniques to eliminate redundancies in the computation of each EVB state and more efficiently parallelize the calculation are necessary to access reasonable time scales and system sizes. The RAPTOR approach[45] and software package for interfacing with the LAMMPS MD engine[48−50] has been created with many of these optimizations in mind as an efficient, ready-to-use implementation of the MS-RMD method. It incorporates, e.g., the MS-EVB 3.2 model for hydrated excess proton transport in water,[25] models for some protonatable amino acids, and proton transport models for several proteins and in a proton exchange membrane. These models often may require only minimal reparameterization in new chemical environments, though the development of MS-RMD force fields is not the objective of the RAPTOR package. RAPTOR also supports a variety of computational and statistical mechanical approaches to accelerate sampling of these reactive systems, allowing for access for multinanosecond to microsecond time scales. The purpose of this paper is to detail these advances and describe how they may be best used in production simulations.

The methods to access longer time scales with the MS-RMD approach may be broadly divided into two categories: first, computational acceleration, which directly speeds up evaluation of the MS-RMD Hamiltonian via more efficient algorithms, more powerful hardware, and well-justified approximations; second, statistical mechanical approaches for enhanced sampling, which uses tools such as metadynamics,[51−55] umbrella sampling,[56,57] and replica exchange[58,59] to explore the potential energy landscape more efficiently. We will begin by describing the MS-RMD algorithm in detail, before moving on to a discussion of computational acceleration approaches, and then statistical mechanical ones. We will then review recent application work and examples of RAPTOR usage, and conclude with a discussion of current and future efforts to further improve RAPTOR and the MS-RMD methodology.

2. METHODS

2.1. The MS-RMD Algorithm. *2.1.1. The MS-RMD Force Field.* The Hamiltonian to describe a reactive system is given by a linear combination of the possible diabatic states, and may be written as

$$H_{\mathrm{RMD}} = \sum_{ij} |i\rangle h_{ij} \langle j|$$

(1)

The diagonal terms, h_{ii}, represent the potential energy of each diabatic state, while the off-diagonal terms h_{ij} reflect the couplings between those diabatic states. At each time step of the MS-RMD simulation, the energies and forces of each nonzero matrix element are computed, and the ground-state energy may be obtained using the secular equation $H_{EVB}\mathbf{c}_i = E_i\mathbf{c}_i$. The eigenvectors $\mathbf{c}_i$ may be thought of as representing the different "weights" associated with each EVB state.

The MS-EVB 3.2 model for proton transport[23,25] uses diagonal terms of the form

$$h_{ii} = V_{H_3O^+}^{\text{intra}} + \sum_k^{N_{H_2O}} V_{H_2O}^{\text{intra},k} + \sum_k^{N_{H_2O}} V_{H_3O^+,H_2O}^{\text{inter},k} + \sum_{k<k'}^{N_{H_2O}} V_{H_2O}^{\text{inter},kk'} \tag{2}$$

Here, $V_{H_2O}^{\text{intra},k}$ and $V_{H_2O}^{\text{inter},kk'}$ reflect the intra- and intermolecular degrees of freedom for the water molecules, and the potentials for these terms directly reflect the underlying water model—in this case SPC/Fw. SPC/Fw is a three-site, flexible water model with an accurate dielectric constant and bulk diffusion properties.[60] The functional forms in the potential follow the traditional representation of terms for bonds, angles, and torsions in the intramolecular potential, and Coulomb and Lennard-Jones terms for the intermolecular potential that are familiar from classical nonreactive force fields. The specific parameters used for the SPC/Fw model may be found in the literature.[60] The term $V_{H_3O^+,H_2O}^{\text{inter},k}$ is the function which governs intermolecular interactions between hydronium and water molecules. It is of the form

$$V_{H_3O^+,H_2O}^{\text{inter},k} = 4\epsilon_{OO_w}\left[\left(\frac{\sigma_{OO_w}}{R_{OO_k}}\right)^{12} - \left(\frac{\sigma_{OO_w}}{R_{OO_k}}\right)^6\right]$$
$$+ 4\epsilon_{HO_w}\left[\left(\frac{\sigma_{HO_w}}{R_{HO_k}}\right)^{12} - \left(\frac{\sigma_{HO_w}}{R_{HO_k}}\right)^6\right]$$
$$+ \sum_m^4 \sum_{n_k}^3 \frac{q_m^{H_3O^+} q_{n_k}^{H_2O}}{R_{mn_k}} + V_{OO_k}^{rep} + V_{HO_k}^{rep} \tag{3}$$

The repulsive terms $V_{OO_k}^{rep}$ and $V_{HO_k}^{rep}$ are two additional repulsive terms which are necessary to correct for an underestimation in the repulsive energy between the hydronium oxygen and water oxygens in the first case, and between the hydronium hydrogen and water oxygen atoms in the second case.[23] This allows for a more accurate description of the potential between the hydronium ion and its first solvation shell. The terms are given by

$$V_{OO_k}^{rep} = B\exp[-b(R_{OO_k} - d_{OO}^0)] \sum_j^3 \exp(-b'R_{H_jO_k}^2) \tag{4}$$

and

$$V_{HO_k}^{rep} = C\exp[-c(R_{HO_k} - d_{HO}^0)] \tag{5}$$

B, b, b', d_{OO}^0, C, c, and d_{HO}^0 are empirical parameters which are fit to higher-level data by iterative force- or energy-matching to *ab initio* calculations. The repulsive terms vanish beyond the first solvation shell, according to a switching function $S(r)$ given by

$$S(r) = \begin{cases} 1, & r < r_s \\ 1 - (r_c - r_s)^{-3}(r - r_s)^2(3r_c - r_s - 2r), & r_s < r < r_c \\ 0, & r > r_c \end{cases} \tag{6}$$

where r_s-r_c is 2.85–3.05 Å for $V_{OO_k}^{rep}$, and 2.3–2.5 Å for $V_{HO_k}^{rep}$.

The functional forms used for the amino acid models are essentially identical, except the classical force field parameters for the amino acid residues,[24,34,47,61] which are procured from the CHARMM force field.[62−66]

The off-diagonal elements characterize the strength of couplings between diabats. Due to differences in electronic structure and protonation behavior between amino acids and water, these terms assume different forms when the coupling is between hydronium and water and between amino acid and water. Since the coupling is determined largely by the geometry near the average proton position, they both include a geometry-dependent term. In the case of amino acids, the coupling may be expressed solely by the donor–acceptor distance and follows a Gaussian form. For example, in glutamates and aspartates, this distance is the distance between the donor oxygen and the excess proton r_{OH}, and the off-diagonal term can be easily computed as

$$H_{ij} = c_1\exp[-c_2(r_{OH} - c_3)^2] \tag{7}$$

Here, c_1, c_2, and c_3 are prefit parameters unique to each amino acid type. The water–water coupling involves a more complicated functional form. For instance, consider the hydronium and water involved in the two diabats forming an $H_5O_2^+$ Zundel ion complex: it can be conceptualized as two water molecules "sharing" an excess proton in between them. Two parameters define the geometry of this complex—the distance between the two oxygens R_{OO}, and a vector $\mathbf{q}$ pointing from the center of the two oxygens to the shared proton. Hence, the off-diagonals can be written as

$$H_{ij} = (V_{\text{const}}^{ij} + V_{\text{ex}}^{ij}) \cdot A(R_{OO}, \mathbf{q}) \tag{8}$$

Here, the geometry-dependent factor $A(R_{OO}, \mathbf{q})$ depends solely on the two above-mentioned quantities. It can be written in closed forms of these two parameters and is facile to compute. Details of this geometric factor can be found in the MS-EVB literature.[23] The prefactor includes a fitted constant V_{const}^{ij} and an exchange term V_{ex}^{ij}. This exchange term represents the Coulomb interaction between the Zundel ($H_5O_2^+$) complex and the environment.

$$V_{\text{ex}}^{ij} = \sum_{m \in \text{complex}} \sum_{n \in \text{env}} \frac{q_m q_n}{R_{mn}} \tag{9}$$

Given the emergence of neural-network force fields, recent work has also considered fitting the off-diagonals in the EVB Hamiltonian to a neural network that is trained on *ab initio* data from the transition state region.[46,67] A neural network reflects a universal approximator for the off-diagonal potential that may better capture effects that are not considered by a predefined analytic form. This provides a key alternative to empirical functional forms for when the nature of the interaction potential is not well-known, or is poorly described by a simple analytic form. However, there do remain important questions to practical implementation of neural network force fields in the MS-RMD method. One particular concern is that,

while still much faster than explicitly computing the electronic structure, neural network inference times are typically on the order of a millisecond, which becomes appreciable when evaluating a large number of terms. This could significantly impact the computational tractability of the model. Additionally, neural network models may not generalize as well as current approaches, or may require exponentially more data to provide accurate, problem-specific results.[34] It remains unclear precisely how much training data would be required to parametrize an accurate neural network force field in a biomolecular context, and this is a key question that must be answered to allow for the routine exploration of complex chemical spaces with a neural network-enhanced variant of MS-RMD.

2.1.2. Evaluation of the MS-RMD Hamiltonian. A crucial component of the multistate EVB scheme is the state-search algorithm which determines how many EVB states to consider at a given time step. At the start of the simulation, a "pivot state" is chosen by considering the proton bound to the closest water molecule. At each time step in the MD simulation, the "pivot state" is reevaluated by considering which state had the largest contribution to the MS-EVB Hamiltonian by its amplitude at the prior time step. The pivot state is then considered as the reactant state, and EVB states are generated, e.g., with each proton from the hydronium ion transferred to each water within 2.5 Å of the respective proton. Each of these EVB states is then considered as a potential reactant state, and the same process is repeated, up until the third solvation shell of the original pivot hydronium is considered. This results in a well-converged EVB state vector—beyond the third solvation shell, a large number of negligible states will be included. This typically results in 15−20 EVB states being considered at each time step for a bulk water excess proton simulation—enough to ensure adequate sampling of reasonable EVB states that the excess proton may occupy, while also maintaining computational tractability. Confined environments typically require far fewer EVB states to model through the third solvation shell. A key insight inherent in this approach to simulating a reactive system is the idea of *charge defect delocalization*. By simultaneously considering a linear combination of the relevant EVB states, one is able to account for the delocalized nature of the excess charge defect and thus explicitly model the Grotthuss shuttling process.[10,11] The key features enabled by MS-RMD modeling of proton transport are presented in Figure 1—first, charge delocalization; and second, Grotthuss shuttling.

The evaluation of the Hamiltonian matrix elements at each time step comprises a majority of the computational cost of the algorithm. Naively, each diagonal element in the matrix is roughly a standard MD cost to evaluate, and the matrix can consist of 20+ nonzero elements in a typical simulation of proton transport in bulk water. Additionally, computing the off-diagonal terms requires summation of the long-range Coulomb interactions. As the number of diabatic states n increases, the computation cost of this exchange term can quickly become significant, given that the number of off-diagonals grows as $O(N^2)$. Traditionally, evaluation of this summation may be accomplished with Fourier space methods, such as particle−particle−particle mesh (P^3M) Ewald summation,[68,69] just like in the diagonal terms.

Scaling properties for a single-proton simulation of the ClC-ec1 protein[33,70] in the 2022.3 release of RAPTOR is presented in Figure 2. A variety of schemes have been implemented to
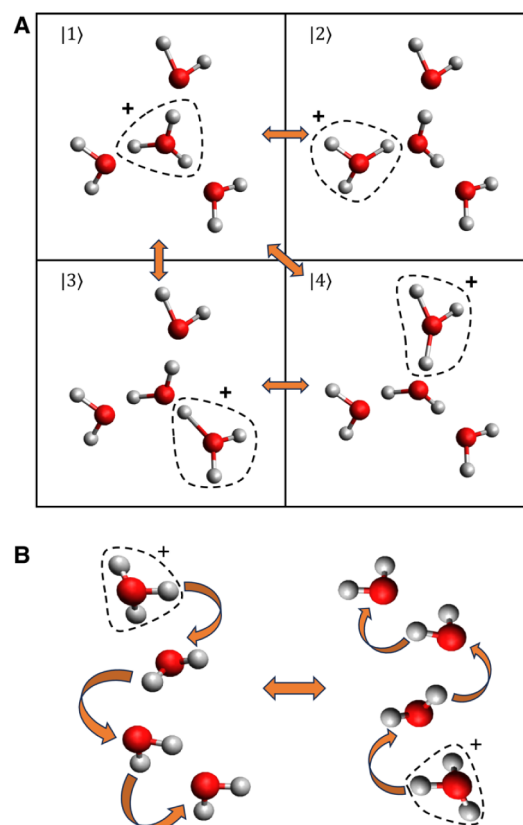

Figure 1. An illustration of the key features of the MS-RMD approach for the excess proton in water. (A) The hypothetical diabatic states considered in an Eigen cation $H_9O_4^+$. By considering the total system to be a linear combination of these localized charge states, the charge defect is effectively delocalized over those states. (B) Grotthuss shuttling in a water wire. The Grotthuss mechanism allows for the excess proton to rapidly shuttle large distances via charge transport in the hydrogen bond network.

remove redundancy and efficiently parallelize the calculation of the matrix elements, which will be detailed in the next section.

With an evaluation of the Hamiltonian elements in hand, one may diagonalize the matrix to obtain ground-state energies, and use the Hellmann−Feynman theorem to compute the forces on each atomic nucleus:

$$F_j^{\text{HFT}} = -\langle\psi_0|\frac{\partial H}{\partial r_j}|\psi_0\rangle = \sum_{m,n} c_m c_n F_j^{mn} \tag{10}$$

which may then be integrated by the MD engine to propagate the simulation forward in time.

2.1.3. Multiple Proton Simulations with SCI-MS-EVB. With RAPTOR, it is also possible to simulate multiple protons (or other reactive species) simultaneously at near-linear scaling.[71] This is achieved with the self-consistent iterative MS-EVB (SCI-MS-EVB) algorithm, which divides the full MS-EVB Hamiltonian with multiple excess protons into complexes whose energies and forces may be solved for independently and then reconciled via an iterative self-consistent process. This is possible, in part, because the reactive complexes make up a relatively small portion of the system at relevant pH values.

Consider a system with two excess protons, partitioned into complex A (containing the first excess proton) and complex B
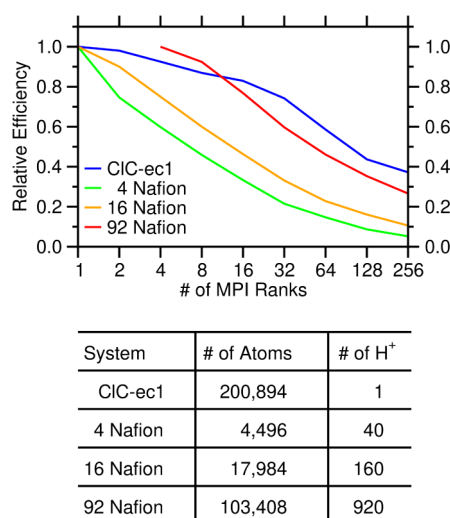
System	# of Atoms	# of H$^+$
ClC-ec1	200,894	1
4 Nafion	4,496	40
16 Nafion	17,984	160
92 Nafion	103,408	920

Figure 2. CPU scaling efficiency of several systems simulated using RAPTOR with MS-RMD and with multiple protons using the SCI-MS-EVB approach. Simulations were run on Cascade Lake Intel CPUs with the 3Nov2022 release of LAMMPS and 2022.3 release of RAPTOR.

(containing the second). We may describe the Hamiltonian for complex A as follows:

$$H_A = H_{AA} + H_{AB'} + H_{AR} \tag{11}$$

where H_{AA} reflects the internal interactions of EVB complex A, $H_{AB'}$ reflects the interactions between particles in complexes A and B, and H_{AR} reflects the interactions of complex A with the nonreactive system.[71] The Hamiltonian for H_B follows as expected. A self-consistent solution may be found by solving for H_A given an educated guess for H_B and then solving for H_B in consideration of that solution, and iterating until convergence is achieved. As with single-proton simulations, the EVB state with the largest weight from the prior time step is used as the initial guess for each complex—for the first time step, a likely hydronium configuration is chosen by considering the excess proton bound to the nearest water. The total system energy is given by

$$
\begin{aligned}
E_{total} &= \langle a_0 | H_{AA} + H_{AR} | a_0 \rangle + \langle b_0 | H_{BB} + H_{BR} | b_0 \rangle \\
&\quad + \langle a_0 b_0 | H_{AB} | a_0 b_0 \rangle + E_{RR} \\
&= E_{AA} + E_{BB} + E_{AB} + E_{AR} + E_{BR} + E_{RR} \tag{12}
\end{aligned}
$$

where $|a_0\rangle$ and $|b_0\rangle$ are, respectively, the ground-state solutions for complexes A and B. The ground-state forces may then be obtained as usual using the Hellmann—Feynman theorem, and the system propagated as shown for the single-proton case. This formalism readily extends to systems with more than two EVB complexes. The SCI algorithm restricts EVB complexes from overlapping, which is a reasonable approximation at dilute to moderate acid concentrations. Scaling properties for the SCI-MS-EVB approach in Nafion proton exchange membrane systems of various sizes are presented in Figure 2. While SCI-MS-EVB scales linearly in cost with respect to the number of excess protons, parallelization properties are worse across multiple nodes than the single-proton case. Scaling properties improve in the larger Nafion systems; however, this is because the general computational load is significantly higher, which better masks the communication overhead.

2.2. Computational Enhancements to MS-RMD. A number of approaches to improve the computational performance of MS-RMD have been developed. The primary computational expense of the RAPTOR algorithm is the computation of the matrix elements at each time step. Domain decomposition and multiple program (MP) parallelization schemes have eliminated substantial redundancies in the evaluation of the MS-RMD matrix elements, which have drastically reduced the cost of evaluating them. These improvements have substantially enhanced the computational performance of RAPTOR, granting it near-empirical MD throughput while remaining accurate enough to provide quantitative estimates of proton transfer rates and pK_a values. Recent efforts have also focused on GPU acceleration and coarse-graining of the electrostatics calculations in the off-diagonal terms.

2.2.1. The CGIS Method. In 2008, Izvekov et al. introduced the Coarse-Graining in Interaction Space (CGIS) method, which force-matched long-range electrostatics into effective short-range potentials with a specified cutoff distance.[72] This approach transforms the k-space summation from an $O(N\log N)$ scaling to a linear scaling based on the system size. Building on this, Yamashita et al. applied the CGIS approximation to compute the exchange term in the off-diagonal elements.[45] They found that substituting the k-space sum in the off-diagonal terms with CGIS short-range forces does not compromise key observables, such as the structure and diffusion of hydrated excess proton in water, radial distribution functions (RDFs) of various atom pairs, and the probability distribution of the RMD coefficients.

However, CGIS off-diagonals were not previously tested with amino acid models. Here, we expanded the method to an "amino acid in water" system, employing the same setup as in Li and Voth.[34] The system includes one glutamate molecule, 241 water molecules, and one excess proton, and the simulation was conducted using 16 Intel Xeon Gold 6248R CPUs. Figure 3A and B illustrates the performance of this system in a well-tempered metadynamics simulation with
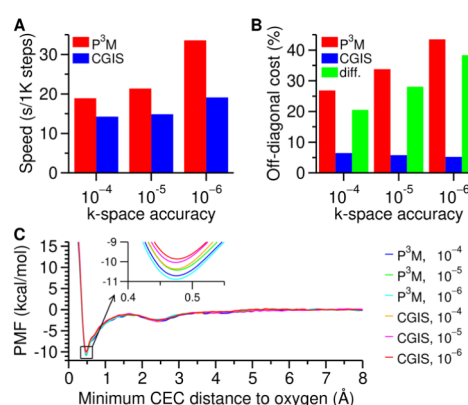

Figure 3. Impacts of RAPTOR off-diagonal evaluation settings. (A) The total time spent on the RAPTOR module using P^{3}M- and CGIS-based off-diagonal calculations at difference k-space accuracies. (B) The percentage of the time dedicated to off-diagonal calculations. (C) Proton dissociation PMF from CGIS- and P^{3}M-based MS-RMD off-diagonals for a glutamic acid in water system at different accuracies. The accuracies of the two treatments of the off-diagonals are comparable. A more detailed look at the well depths and associated uncertainties is available in Figure S1.

various k-space summation cutoffs. As the required P^3M accuracy increases from 10^{-4} to 10^{-6}, the costs of off-diagonal computation escalates rapidly, both in absolute time (Figure 3A) and as a percentage of the total cost (Figure 3B). At a force accuracy of 10^{-6}, calculating off-diagonal terms with P^3M can take 43.4% of the total time used by RAPTOR, while the time on CGIS remains relatively constant. At various accuracies, switching from P^3M to CGIS off-diagonals can save from 24.8% to 43.1% of the overall time consumed by RAPTOR.

Figure 3C shows the proton dissociation PMFs in water computed from both glutamic acid models. All curves were shifted to ensure that the free energy decays to zero at large distances. The curves show similar profiles, both in terms of well depth and asymptotic behavior. When using P^3M with 10^{-4} accuracy (the conditions under which the glutamate model was parametrized) the well depth is 10.7 ± 0.2 kcal/mol ($pK_a = 3.95$), and when using CGIS with the same accuracy, the well depth is 10.4 ± 0.3 kcal/mol ($pK_a = 3.65$). Both the well depth and pK_a compare favorably with each other and with experiments ($pK_a = 4.07$). Over the course of the metadynamics simulations, 5 PMFs were extracted to calculate the standard error. These detailed uncertainties are shown in Figure S1. We note that the MS-RMD model using CGIS could be easily reparametrized to give a more accurate pK_a value.

2.2.2. Parallelization via Domain and State Decomposition. The primary parallelization method available in LAMMPS is domain decomposition, in which the simulation box is divided into nonoverlapping domains whose interactions may be computed in parallel. Each domain is assigned to a unique Message Passing Interface (MPI) process which updates the atom positions, velocities, and forces at every time step. The domain decomposition approach is highly efficient for short-ranged interactions because atom information is communicated between neighboring MPI processes. Based on the outcome of the EVB state search process, the full system is partitioned into an "environment" region, containing all atoms not involved in an EVB state, and a "complex" region, containing the atoms involved in EVB complexes. The environment-environment interactions are only computed once per time step by LAMMPS. As a result, the major computational overhead of RAPTOR concerns environment–complex and complex–complex interactions. As the complexes concern a small portion of the system, the bonded interactions are relatively cheap, so the primary computational cost comes from the electrostatics. The neighbor lists that LAMMPS builds to handle the electrostatics may be reused, with appropriate sorting, to reduce the cost of recomputing the electrostatics for each EVB complex.

Domain decomposition comprises a substantial source of RAPTOR's parallel efficiency—as the computations for the bonded and short-range nonbonded interactions are truncated, they need only be computed once per time step for the nonreacting atoms which comprise the majority of the simulation volume and do not change between the diabats. This dramatically reduces the overall computational cost of MS-RMD compared to the naïve case by rendering the scaling of the intramolecular and short-range nonbonded interaction computations with respect to the number of diabatic states essentially linear. The extent of parallelization possible with this approach is primarily limited by evaluation of the long-range electrostatics.

Efficient parallelization of the long-range nonbonded interactions remains a major challenge, as the $1/r$ Coulomb sum decays too slowly to make reasonably small domains viable. Despite formally scaling as $O(N \log N)$, the reciprocal space component scales poorly at high processor counts as expensive all-to-all communications are required to communicate the electrostatic information from the P^3M grid to each processor. This cost degrades performance significantly at high state counts, such that the reciprocal space portion begins to dominate the overall compute time.[45] This comprises the main computational bottleneck to RAPTOR's performance and parallelization at high state and MPI rank counts. As a result, additional parallelization schemes at the MPI and OpenMP levels are also considered, in addition to approximations of the long-range electrostatics which reduce the number of long-range fast Fourier transforms (FFTs) required.

The suboptimal scaling of the long-range electrostatics computation may be limited by considering a multiple program (MP) scheme. In the MP scheme, a small subset of the processors are assigned the communication-intensive long-range electrostatics computation, while the rest of the processors handle the real-space bonded and short-range electrostatics terms.[73] This contrasts the more conventional single program, multiple data (SPMD) parallelization paradigm, where the same set of tasks are performed on different sets of data. An MP scheme has been implemented for RAPTOR in LAMMPS, resulting in significantly improved parallel scaling at high processor counts.[74] The primary advantage of the MP scheme is that one significantly reduces the number of MPI ranks involved in the required all-to-all communications for the P^3M grid. A 3:1 ratio between the real-space and reciprocal-space partitions is typically used.[75] The primary overhead cost of this approach is that communication is required between partitions that are computing the real-space and reciprocal-space terms for the same simulation volume. Therefore, MPI rank reordering is needed to ensure that those communications are intranode. The cost of this load balancing scheme is typically only worthwhile at high processor counts—the MP scheme typically begins to see improved performance at >128 cores.[45,73]

A similar principle to domain decomposition may be applied to achieve state decomposition, where the computations for each diabatic state are conducted in parallel. This is implemented as an additional layer of parallelism on top of domain decomposition and OpenMP multithreading. State decomposition simply involves exploiting the obvious source of parallelism inherent in the MS-RMD approach: it computes the interactions for different diabatic states on separate MPI ranks. Specifically, LAMMPS is run in partitioned mode, which uses MPI_Split operations to create new MPI subcommunicators for each partition. The partitions are given the same particle coordinates and velocities, so that they obtain the same MS-EVB states after independently running the state search algorithm. A static load balancing algorithm determines which state each partition will compute. Following evaluation, an all-to-all MPI communication process produces the Hamiltonian, which is diagonalized by each partition to give the ground state MS-EVB energy and the corresponding eigenvectors. Forces are then obtained via the Hellmann–Feynman theorem as discussed previously. Following force evaluation, an all-to-all MPI synchronization is required, as each partition only has access to the matrix elements it has evaluated. However, the spatial decomposition may be leveraged here by performing

the communication within a MPI communication group that contains the same spatial domains.[73] The forces can then be propagated by the MD integrator, providing new coordinates and velocities for the next time step. Compared with the domain decomposition scheme, state decomposition is not especially productive at low node counts, owing to the dynamic evolution of the number of states and the high overhead associated with load balancing. State decomposition also inherently reduces the number of MPI ranks available to domain decomposition, which is a more efficient source of parallelization in most cases. State decomposition does, however, yield significant performance improvements for SCI-MS-EVB simulations.[42]

Parallel performance at the shared-memory level is implemented with the OpenMP API as a force decomposition scheme. This allows for a variety of loop-level parallelisms to be implemented; for instance, the pairwise additive force computations may be distributed across multiple threads, as well as the bonded interactions and certain portions of the long-range electrostatics computation, such as interpolating charges onto the P^3M mesh. The implementation of this parallelism for RAPTOR uses LAMMPS's implementation for the diagonal matrix elements, and is adapted to the RAPTOR-specific evaluation of the off-diagonal elements. Typically, this parallelization is only effective at extremely high MPI rank counts.[73]

2.2.3. GPU Acceleration of MS-RMD. The fine-grained, automatic-scaling parallelism available in general-purpose graphics processing units (GPGPUs) allows for additional performance gains on top of what is possible with the domain and state decompositions. Efforts to accelerate RAPTOR with GPGPUs in LAMMPS have been active since the MS-EVB2 version. Our implementation is based on the framework of the GPU package,[76−79] where the bottlenecks of a MD time step, that is, nonbonded force and energy evaluations, are performed on the GPU. The long-range electrostatic solvers and bonded interactions are computed concurrently on the CPU. This hybrid MPI/GPU approach proves efficient for computationally expensive force fields since it allows multiple MPI processes to saturate the computing capacity and memory bandwidth of the GPUs.

Our findings for optimizing the performance of the GPU-accelerated MS-RMD in the RAPTOR package can be summarized as follows. First, we found that it is beneficial to off-load only the nonbonded and real-space electrostatic forces and energies that involve the environment atoms to the GPU. The short-range contribution to the electrostatic energy of the diagonal elements of the Hamiltonian matrix remains on the CPU. This partial offloading strategy significantly reduces number of host-device data transfers required for the atom neighbor lists corresponding to individual bonding states. Further reduction in the host-device transfers comes from the fact that we only need to update the neighbor list of the environment atoms on the device when the host counterpart is modified upon enumerating over the bonding states. To compute the force of each atom on the device, we distribute the iteration over its neighbor list across multiple GPU threads to ensure that all the streaming processors are occupied and to reduce the number of iterations per thread.

Second, the reciprocal space contribution to the electrostatic energy of the bonding states of a given complex can be evaluated with a separate mesh rather than with the original grid that spans the whole simulation box. As suggested by

Yamashita et al.,[45] it is possible to use a coarser mesh for the complex atom charge density without noticeable changes in the accuracy. Because the P^3M relative error is estimated based on the sum of the squared charges, we notice that the number of grid points needed for quite a few reactive atoms for a given accuracy can be smaller than that of the grid for the whole system. This is important because the computational cost for the long-range contribution to the bonding state energies can be reduced.

Third, the reciprocal space contribution to off-diagonal matrix elements can be approximated by damped shifted force, Debye screening, or similar truncation schemes. This is possible because the off-diagonal terms are smaller than the diagonal terms by an order of magnitude and a careful treatment of the approximation such as the Wolf summation is sufficient for capturing the long-range contribution.

To demonstrate the performance gain with GPU acceleration, we chose a system that is representative of biological simulation studies in practice: a solvated Cl^-/H^+ antiporter protein from *E. coli* (ClC-ec1) with an excess proton, consisting of 200,894 atoms in total. The CHARMM22[62,80,81]/CMAP[63,64] force field was employed. The electrostatic interactions were computed with a short-range cutoff of 12 Å, with the long-range contributions treated by the P^3M method with a relative accuracy of 10^{-5}. Both systems were first equilibrated for 500 ns in the canonical ensemble at T = 300 K using a Nosé−Hoover chain thermostat.[82] The benchmark simulations were conducted for 100 MD steps with a time step of 1 fs. The atom neighbor list was rebuilt every 5 timesteps with a buffer of 2 Å.

Figure 4A shows the strong scaling performance of the GPU accelerated version vs the non-GPU version on a single node. The CPU-only and GPU-accelerated versions exhibit good scaling, indicating that the parallel performance within a node is computation bound for the system size under investigation. The GPU speedup vs the MPI-only version increases with the
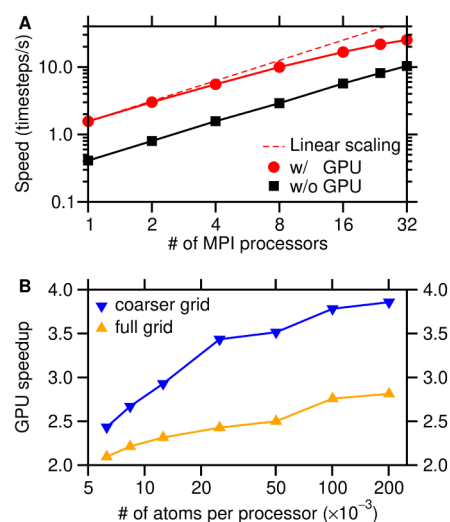

Figure 4. GPU acceleration of RAPTOR. (A) Strong scaling performance of the RAPTOR code with and without GPU acceleration on a single node with up to 32 CPU cores of a solvated protein and single-site proton transfer. (B) GPU speedup vs MPI-only version as a function of the number of atoms per processor. The GPU-accelerated data are collected from the optimal setting at a given number of MPI processes.

number of atoms per processor. The GPU speedup is significant at the lower MPI counts because the number of atoms per process is high, and thus the workload is primarily due to the computation of the real-space contribution that is done to the GPUs. By tuning the buffer size of the neighbor list and the number of GPU threads used for tallying atom forces and energies, we observe a significant boost in the performance. Specifically, using an increased buffer size of 3 Å and 32 GPU threads per atom (the whole SIMD vector length, or CUDA warp size) the timing for the short-range and real-space interactions between the environment atoms is reduced by orders of magnitude when offloaded to the GPUs: e.g., from 26.0 to 0.3 s on 8 MPI processes sharing a GPU. The adjustment in the neighbor list buffer size and GPU threads per atom is motivated by the need to reduce the host-device neighbor list transfers and the fact that the average number of neighbors per atom is around 650 for the real-space cutoff of 12 Å.

As the number of MPI processes increases, the number of atoms per process decreases while the communication overhead for gathering the charge densities on the grid between the processes increases. For the full-node 32-MPI runs without the GPUs, the timing due to the reciprocal space calculation, and more precisely, the communication overhead needed for the P^3M calculations, accounts for approximately 24% of the total simulation time. With GPU acceleration, this non-GPU part becomes the bottleneck, reaching 90% of the total simulation time. Consequently, the GPU-accelerated runs deviate from linear scaling, maintaining 78% parallel efficiency.

The effects of using a coarser grid for the P^3M solver for the long-range contribution to the electrostatic interactions between reactive atoms are shown in Figure 4B. For the benchmark system, the simulation box dimensions are 118 × 115 × 237 Å. With the relative RMS force error of 10^{-5}, we need a P^3M grid composed of 72 × 72 × 128 points along the x, y, and z dimensions. This full P^3M grid is employed to evaluate the long-range force and energy for the environment atoms. A coarser grid of 36 × 36 × 72 points is needed for 28 reactive atoms to give the same order of magnitude relative error given the box dimensions. Using this coarse grid for the reactive atoms, we found a strong boost in performance across all the number of CPU cores: from 50% speedup at low atom counts to 100% speedup at high atom counts.

The reasonable GPU speedup at intermediate MPI counts (4−8 processors) provides opportunities to obtain higher aggregate throughput at the node level. By packing independent simulations each occupying a subset of CPU cores and GPUs, one can harvest higher aggregate simulated times as compared with using a non-GPU full-node simulation or using a single simulation with 4 GPUs. We found that by packing 4 simulations each using 8 CPU cores and 1 GPU into one node, the aggregate timesteps are 4.5× higher than using a single simulation with 32 CPU cores without the GPUs, and 2× higher than using a single simulation with all the 4 GPUs in the node. The ability to accelerate individual runs in parallel is also important for enhanced sampling that involves replica exchange.

2.3. Enhanced Sampling with MS-RMD. 2.3.1. Collective Variables for Proton Transport.
It is commonly the case that computational acceleration alone is not enough to access the reactive pathways of interest in MS-RMD simulations, particularly if such a pathway reflects an energetically unfavorable rare event. In this case, statistical mechanical biasing along a collective variable (CV) that describes the reaction pathway is required. RAPTOR and LAMMPS may be interfaced with the PLUMED software package to conduct such enhanced sampling, just as one might do with a typical classical molecular dynamics simulation.[83,84] However, different rules and constraints apply when choosing CVs for MS-RMD simulations. Additionally, there are differences between the various common enhanced sampling techniques (metadynamics, umbrella sampling, and replica exchange) which are worth discussing in a MS-RMD specific context.

Given the delocalization of the charge defect among multiple EVB states in the MS-RMD framework, it is essential to define a variable that best reflects the effective position of the excess protonic net positive charge. This is given by the center of excess charge, or CEC, defined as

$$r_{CEC} = \sum_i^N c_i^2 r_{COC}^i \tag{13}$$

where c_i^2 is the magnitude of the ith EVB state vector, and r_{COC}^i is the position vector of the center of charge of the hydronium for the respective EVB state.[22,85] This allows for one to readily compute a mean squared displacement (MSD) that tracks the position of the excess proton over time. It also provides an avenue to bias the simulation, via a path-dependent CV that describes the distance of the CEC from a key protonatable residue. In a simple situation, such as that of a glutamic acid residue in bulk water, the reaction coordinate can simply be described by the distance between the CEC and the closer glutamic acid oxygen,[34]

$$\xi_{CEC}^{Glu} = -\frac{1}{\kappa} \log[\exp(-\kappa(r_1 - \overline{r})) + \exp(-\kappa(r_2 - \overline{r}))] + \overline{r} \tag{14}$$

For this CV, κ is a constant equal to 40 Å^{-1}, r_1 and r_2 describe the separation between the CEC and the two respective carboxyl oxygens, and $\overline{r}$ is the average separation.

MS-RMD simulations of amino acids almost always require biasing along a CV similar to the one described above, which drives the simulation toward sampling the relatively rare protonation and deprotonation events. In bulk water, a CV based on the CEC distance is typically sufficient to describe sampling of these events. However, in many systems of chemical interest, additional CVs are needed to fully sample the relevant free energy space.[32−34,86,87]

In confined environments, such as in protein channels, membranes, and pores, water connectivity is starkly different, and a CEC-based CV is alone insufficient to approximate the reaction coordinate. Confined environment water connectivity has often been described according to "water wires": single-file arrangements of water molecules that enable the Grotthuss shuttling of protons through confined spaces.[86] Under these conditions, a novel CV—one which accurately describes water wire connectivity—may be required. The resulting CV should be continuously differentiable, and derived directly from a structural assessment of water wire connectivity in the presence of an explicit excess proton, given that the presence of the excess proton will considerably distort the water lattice.[86] Li and Voth derived such a CV from graph descriptions of water wire networks, namely by looking at the principal curve connectivity.[86] This provides an avenue to quantitatively sample the transport capacity and route of a given water wire structure in the presence of an excess proton.

This water connectivity CV is implemented in a custom modification of PLUMED which is available upon request, and described herein below.

The principal connectivity variable, ϕ, may be regarded as a "coarse graining" of the water wire structure. First, a smooth water coordination number is determined for each bead, which reflects the solvation of all water oxygens (x_i):

$$s_i = \sum_{l}^{N_w} f_{sw}(|x_l - x_i|) \tag{15}$$

The switching function f_{sw} is of the form

$$f_{sw} = \begin{cases} 1, & x < d_0 \\ \left(\frac{(x - d_0)}{r_0} - 0.5\right)\left(\left(2\left(\frac{(x - d_0)}{r_0} - 0.5\right)\right)^2 - 1.5\right) + 0.5, & d_0 \leq x \leq r_0 \\ 0, & x > r_0 + d_0 \end{cases} \tag{16}$$

which allows for the water wires to fluctuate somewhat around the principal curve, but avoids introducing a change to the final value of the CV. The next task is to define a variable that describes the connectivity of the system, analogous to an adjacency matrix in the all-atom case. The occupancies l_i, ranging from 0 to 1, may be given by the Fermi relation,

$$l_i = \frac{1}{1 + \exp\left(-\frac{s_i - s_w}{\sigma}\right)} \tag{17}$$

where s_w and σ reflect the degree of occupancy of a given bead based on its coordination number. Given that two adjacent beads on the graph will be connected when they are both occupied, the two-body connectivity $f_{i,i+1}$ may be described as $(l_i + l_{i+1})/2$. The curve will be fully connected if all of the two-body pairs are connected, and so the full principle curve connectivity CV ϕ may be written as the product of each respective two-body connectivity,

$$\phi = \left(\prod_{i=1}^{N-1} f_{i,i+1}\right)^{1/(N-1)} \tag{18}$$

CEC-based and water wire-based CVs provide an excellent starting point for modeling a reaction coordinate for proton transport in proteins, but in many cases system-specific CVs are needed to characterize conformational changes that allow for protonation events to occur.[34,61] Typically, these CVs are based on the conformation of larger protein subassemblies or the positioning of key residues or functional groups. These secondary CVs are usually highly system-specific, and are determined based on observations from unbiased simulations.

2.3.2. Simulation Biasing Methods with MS-RMD. The two most commonly used methods to bias a MS-RMD simulation are metadynamics[51−54] (MetaD) and umbrella sampling[56,57] (US). Depending on the quality of the CVs available and the character of the system's free energy surface, the two methods offer trade-offs which are worth discussing in the context of MS-RMD simulations.

MetaD is commonly used with MS-RMD simulations when there is only one CV of interest and the character of the free energy surface is not well-known.[54] In particular, well-tempered MetaD (WT-MetaD)[52,54,55] and transition-tempered MetaD (TT-MetaD)[53] have proven to be especially valuable for MS-RMD given their ability to precisely estimate the free energy surface, and in the case of TT-MetaD, converge faster. MetaD may also be employed in a multidimensional form if there are more than one CVs of interest that describe the reaction coordinate. However, as the number of CVs grows larger, it becomes more difficult to converge the free energy surface. More than two CVs are rarely used in practice.

If all states of reactive interest are known, TT-MetaD provides a method to more efficiently capture the nature of the free energy landscape between those states. TT-MetaD, which was formulated by Dama et al. in 2014, is a hybrid approach that combines the advantages of both standard and well-tempered MetaD. It arises from the recognition that MetaD is essentially a two-stage process—in the first, the hills fill the metastable basins in the energy landscapes. Once those basins are filled, and the energy surface is similar in composition across the landscape, the system will diffuse across the free energy surface. During the first phase, TT-MetaD functions similarly to conventional MetaD, as Gaussian hills of the same size are deposited on the surface. Once the basins of the free energy surface are filled, tempering is added to achieve convergence. This minimizes the overall time to convergence by combining traditional MetaD's faster basin filling with WT-MetaD's more efficient convergence of the free energy surface. Naturally, this approach requires a way to determine when all of the basins are filled, and the second phase of MetaD has begun. This is accomplished by looking for where the bias potential is linked across all of the major basins in the free energy surface—that is, there are no points along the free energy surface connecting any states of interest where the bias potential is zero.[53] As such, successful use of TT-MetaD requires some *a priori* knowledge of the states of interest, and the method is primarily useful for providing information on the transitions between them. Like with WT-MetaD, the decaying exponential guarantees asymptotic convergence in the second phase.

Typically, TT-MetaD will converge more rapidly than WT-MetaD and standard MetaD given a reasonably appropriate CV or set of CVs. As with any enhanced sampling method, the convergence of the free energy surface is essential, and in many cases it can be challenging to achieve convergence with any form of MetaD. A common problem that arises in MS-RMD simulations where one has two linked CVs is that one CV will often be much faster converging than the other, if for instance one CV is related to CEC position and the other is related to protein conformation. The time scale mismatch between the fast proton transport CV and the slow protein conformation CV leads to slower convergence of the overall two-dimensional free energy surface. While MetaD remains the enhanced sampling method of choice in MS-RMD simulations where there is to be biasing along a single reaction coordinate, in instances where there are two or more CVs (and those CVs have different time scales) two-dimensional umbrella sampling (2D-US) is often required due to its more robust convergence properties.[57,88] This comes at the expense of a less complete sampling of the free energy surface when compared with MetaD, especially if the CVs chosen do not fully characterize the reaction coordinate.

It should be clear that the choice between US and MetaD is one between control over the reaction pathway (and thus more facile convergence) versus a more complete sampling of the

free energy space (and thus slower convergence). In other words, if the user has knowledge of (or a reasonable guess for) the reaction pathway based on their CVs, US is the most direct way to sample that path. However, this comes at the cost of potentially neglecting pathways or regions of the free energy surface that are not perfectly considered by one's chosen CVs. Additionally, 2D-US tends to be more computationally intensive for a given amount of simulation time compared with MetaD, as many umbrella windows are needed with significant overlap between them to ensure the CV is adequately sampled.[33,47,57] Each window may be run independently, however, allowing for efficient parallelization.

2.4. Analysis of MS-RMD Trajectories. A number of techniques may be used to analyze the output of MS-RMD trajectories to obtain properties such as the protonation barrier and reaction kinetics. The RAPTOR software distribution offers a Python-based analysis suite, "raptoranalysis", for interpreting LAMMPS and RAPTOR outputs. This module facilitates trajectory parsing through classes "LammpsReader" and "RaptorReader", enabling users to efficiently filter and parse simulation trajectories. In addition, it includes functions for calculating the mean square displacement (MSD) of the center of excess charge (CEC), analyzing proton hopping events, and assessing proton transfer mechanisms through MS-RMD coefficients analysis. Additional functionalities include evaluating the radial distribution functions and providing insights into the stability of hydrated proton forms via EVB coefficient statistics. In addition, the suite includes Jupyter notebook examples with detailed explanations to guide users in analyzing single and multiproton systems with the module. More information on the raptoranalysis module is available in the Supporting Information.

To ascertain the PMF from an enhanced sampling simulation, one will use a free energy estimator appropriate for the enhanced sampling method used as described earlier. For MetaD, this is simply a matter of summing the Gaussian hills appropriately to determine the contours of the free energy surface.[54,88] With US, exponential averaging methods such as the weighted histogram analysis method (WHAM)[89,90] and discrete transition-reweighted analysis method (dTRAM)[91,92] are typically used to construct the free energy surface. In order to determine the minimum free energy pathway through the PMF, the string method may be used.

The rate for proton transport can then be estimated using transition state theory:[32,93]

$$k_{rxn} = \frac{\omega_0}{2\pi} \exp\left(-\frac{\Delta F^{\ddagger}}{k_B T}\right) \tag{19}$$

where $\Delta F^{\ddagger}$ is the free energy barrier height along the minimum free energy path, and ω_0 is the fundamental frequency of the reactant state oscillations around its minimum, which is given by

$$\omega_0 = \sqrt{\frac{\partial^2 PMF(r)/\partial r^2}{m_{eff}}} \tag{20}$$

where m_{eff} is determined using the equipartition theorem, i.e., $m_{eff}\langle v^2 \rangle/2 = k_B T/2$, where the value of $\langle v^2 \rangle$ is computed from the MS-RMD trajectory sampled at r_0. It should be noted that more elaborate forms of TST may also be employed,[32,94] including two-dimensional versions that include a second CV beyond the CEC.

3. RECENT APPLICATIONS OF MS-RMD

Recent applications with the MS-RMD method cover a wide range of chemically and biologically relevant systems. In particular, the method has been instrumental in the effort to elucidate a definitive answer of the structure and dynamics of the charge defect in bulk water, which had been a major outstanding question in the physical chemistry community for a number of years.[7,25,95] In addition, MS-RMD has provided insight into proton transport at air–water[29,30,96,97] and water–oil[98] interfaces, in materials systems including carbon nanotubes (CNTs)[13,99] and the Nafion perfluorosulfonic acid (PFSA) membranes,[38,40,42,100−103] and in a number of biologically relevant protein systems, including but not limited to the enzyme staphylococcal nuclease from *S. aureus* (SNase),[34,61] the Cl⁻/H⁺ antiporter from *E. coli* (ClC-ec1),[32,33] cytochrome *c* oxidase (C*c*O),[36,37] the multidrug transporter EmrE from *E. coli*,[104] and the influenza A M2 proton channel (AM2).[12,35,105−107] This section will detail scientific insights and advances in these applications (and others) which have been made possible by MS-RMD.

Absolutely critical to MS-RMD's success in defining the structure of the excess proton in bulk water is its ability to explicitly model Grotthuss shuttling, on long time scales and with the appropriate proton charge defect delocalization. To our knowledge, MS-RMD is the only method currently available to model excess proton delocalization and shuttling while simultaneously being efficient enough to routinely access nanosecond to microsecond time scales. This grants it unique insight into both the solvation structure and structural reorientation dynamics of the excess proton. By delocalizing the charge across many EVB states, one accurately captures the quantum-like effects which cannot be captured by a fixed bonding topology MD. MS-RMD simulations,[7,17] in conjunction and agreement with ultrafast nonlinear spectroscopy, have established that a dynamic and distorted Eigen cation, $H_9O_4^+$, is the primary structural motif of the hydrated excess proton in bulk water. In addition, MS-RMD results have suggested that the hydrated excess proton rapidly changes partners in the "special pair dance", which characterizes the distortion of the Eigen complex.[95] This process occurs on time scales of tens of femtoseconds, which is too rapid to be readily apparent from current ultrafast spectroscopy results.[7] MS-RMD simulations have therefore been instrumental in capturing the structure and dynamics of the excess proton defect in bulk water.

MS-RMD has also been used to explore the effects of charge defects at the air–water interface.[29,30,96] Crucially, MS-RMD simulations have demonstrated that the hydrated excess proton has a small affinity for the air–water interface, while the hydroxide ion is repelled from it. In the case of the excess proton, this is due to a favorable enthalpic contribution due to elimination of the charge defect in the hydrogen bond network caused by the presence of the proton in bulk—the resulting increase in water–water interactions creates a favorable, negative enthalpic contribution. In the case of the hydroxide, it is enthalpically repelled from the air–water interface, which is due to a reduction in energetically favorable ion–water interactions.[29] Experimental work[108,109] has corroborated the affinity of the excess proton for the air–water interface, in agreement with the prediction first made with MS-EVB simulations in 2004.[96] Additional work on the air–water interface has explored the effect of the definition of the air–

water interface on the surface affinity of the excess proton.[97] At the oil–water interface, MS-RMD simulations have also been used to elucidate changes in the structure and dynamics of charge defects.[98] At a neopentane–water interface, MS-RMD simulations showed that the hydronium cation has a stabilizing effect on the hydrophobic solutes in the aqueous phase, and has a significantly lower transfer free energy compared to a sodium cation.

MS-RMD simulations have also been used extensively in a wide range of protein environments to elucidate the mechanics of proton shuttling and how those mechanics impact broader structural rearrangements. The ability to explicitly consider the protonation of key amino acid residues simultaneously with Grotthuss shuttling through the hydrogen bonding network is key to its insight. Three systems in particular have been explored extensively: the ClC-ec1 antiporter, which is responsible for a variety of cellular processes such as maintenance of the membrane potential and pH regulation;[70,110] C*c*O, a key proton pump in the respiratory chain of mitochondria and bacteria;[111,112] and influenza AM2, which transports protons across the viral membrane and catalyzes a dissociation of the viral matrix proteins which is essential to the virus replication cycle.[113,114] In all three of these systems, proton transport regions shuttle protons to and from key amino acid residues buried within the protein.

Proton transport through confined environments is a very different process from proton transport in bulk. The carbon nanotube (CNT) system offers a simple system in which one can understand the basic effects of confinement on proton transport. The findings from the CNT system are 3-fold: first, proton delocalization significantly lowers the barrier of transport through the CNT. Figure 5 presents the transport of a CEC-delocalized excess proton versus that of a classical hydronium cation (with no Grotthuss shuttling) through the CNT. The free energy barrier of transport through the CNT is ~2 kcal/mol lower with the CEC excess proton versus the classical hydronium, showcasing the need to model a delocalized proton to achieve an accurate idea of the energetics. Second, contrary to the belief that protons will hop only after the prior establishment of a water wire, MS-RMD simulations have demonstrated that hydrated excess protons can actual dynamically hydrate dry regions of pores and channels by forming their own transient water wires.[13,99] The corresponding 2D PMFs using a CEC-based CV and a water occupancy CV, or using a CEC-based CV and water connectivity CV, both demonstrate the dynamic formation of transient water wires in carbon nanotube systems.[13,86] Third, the geometries of CNTs can impact their selectivity for different ions. CNTs simulated with MS-RMD at a number of different pore sizes and lengths showed that the CEC-delocalized cation diffuses much more rapidly than a potassium cation, that the spatial distribution of waters within the pore vary significantly based on the pore size, and that Zundel cations are typically more favored in larger nanotubes.[99] These results conclusively demonstrate that Grotthuss-assisted diffusion (as opposed to vehicular diffusion) is important to proton transport through a water wire. The CNT system additionally provides a key case study on the substantively different structural and diffusive properties that will emerge in confined environments with proper modeling of the charge delocalization defect. The basic features of proton transport in this system are also transferable to more complex systems.
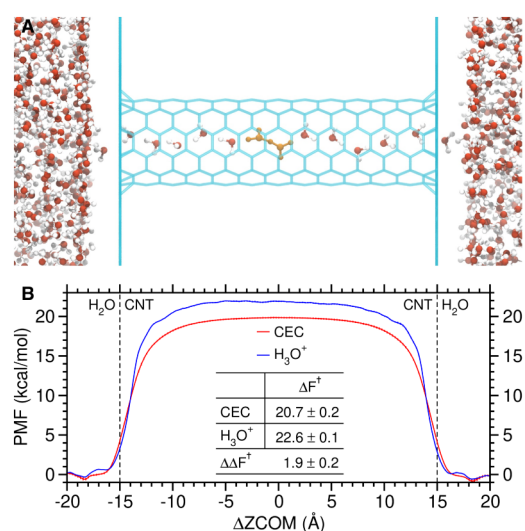

Figure 5. Effects of explicit Grotthuss proton transfer in simulations. (A) Proton transport through a 30-Å (6,6) carbon nanotube (CNT). Cyan lines depict the CNT and two graphene layers. Water molecules are shown as ball-and-stick models. A single water wire connecting bulk waters via the CNT is visible, with orange highlighting the excess proton (CEC) delocalized across two water molecules. For clarity, ions are not shown. (B) Potential of mean force (PMF) profiles of CEC (red line) and classical hydronium ion with no Grotthuss hopping (blue line) through the CNT. Simulation settings followed Ma et al.[99] Black dashed lines mark the entries of CNT. PMFs were averaged from three independent runs with error bars indicating standard deviations. Included is a table of free energy barriers ($\Delta F^{\ddagger}$s) and their difference ($\Delta\Delta F^{\ddagger}$).

Influenza AM2 is critical to regulating the life cycle of the Influenza protein. In the activation process, proton permeation acidifies the virion to catalyze the release of viral RNA.[113,114] MS-RMD simulations have been critical in characterizing both the function and free energy profile of this process and also characterizing how antiviral drugs may inhibit its function.[12,35,105−107] MS-RMD simulations coupled with QM/MM have offered essential, atomic-level insights into the gating mechanism of the His37 tetrad. Specifically, these simulations have offered key insight on a longstanding debate over whether the His37 tetrad functions via a "shutter" or "shuttle" mechanism—that is, whether it functions as a gate, opening at low pH due to electrostatic repulsion between the doubly protonated histidine residues, or whether the His37 tetrad actually changes protonation states and shuttles the proton through the His37-Trp41 region.[35] MS-RMD simulations of proton transport through water chains were key to describing the energetics prior to and after the His37 tetrad while QM/MM was used for the tetrad region. Combined, the overall PMF from these simulations showed that the excess proton must overcome a large energy barrier but is then heavily stabilized as the proton is delocalized and bound into the His37 tetrad and then released. This also explains the pH-dependent activation of the channel—by lowering the pH conditions, the deprotonation barrier of the His37 tetrad is lowered, leading to channel activation. The simulations also help to explain how pH gradients between the virion environment and bulk help explain proton flux behavior.[35,105]

Additional work on AM2 has focused on conformation changes in the protein environment, which accompany the presence of an excess proton.[12] Explicit modeling of the excess

proton with charge delocalization has a profound influence on both protein conformation and the water hydrogen-bonding network in the channel. In particular, the excess proton is found to shift the protein structure conformation away from equilibrium according to the position of the excess proton. In addition, the distribution of excess protons around the channel is shown to be asymmetric, with implications for drug design and mechanistic insight. Following this, MS-RMD simulations were used to explicitly model the binding of an adamantyl amine inhibitor to M2 in the presence of an excess proton.[106] These simulations demonstrated that the ammonium group on the inhibitor leverages the channel's natural ability to stabilize excess charge, and thus effectively acts as a hydronium mimic. Additionally, they showed that the drug binding pocket, located in a particularly stable and symmetric portion of the channel, is particularly conducive to binding near-spherical drugs. Furthermore, the D44N mutant of AM2 has been studied with MS-RMD.[107] It was found that the mutation significantly lowers the barrier of His37 deprotonation, and that this effect is supported by structural shifts that facilitate more facile transport of protons in the viral interior. In short, it should be clear that MS-RMD simulations have been critical to furthering our understanding of the function and activation of the AM2 channel, by allowing for the explicit modeling of a fully delocalized protonic defect on multiple-nanosecond time scales.

In the ClC-ec1 system, extensive MS-RMD simulations have provided a detailed picture and understanding of the proton transport mechanism at atomic resolution.[32,33] Using 2D-US, MS-RMD was able to provide a complete free energy profile of the proton transit process. 2D PMFs as a function of the excess proton CEC and the water occupancy in the central region of the protein help elucidate the reaction mechanism and pathway of proton uptake through the channel. In particular, MS-RMD results suggest that proton transport in the central region of the ClC-ec1 protein can be induced by, but does not strictly require, the presence of a Cl⁻ anion in one of the crystallographically resolved anion binding sites. As it is experimentally well-known that proton and Cl⁻ transport occur in tandem, these results suggest that the coupling occurs elsewhere in the proton uptake process. Further work with MS-RMD on the system has demonstrated the crucial role of the deprotonation of glutamic acid E148 in facilitating proton transfer from bulk to intracellular solution.[32] In particular, it is shown that the deprotonation of E148 is the rate-limiting step for proton transport, and that this step is significantly accelerated by the presence of a Cl⁻ anion in the central region of the protein. In the absence of the central Cl⁻, E148 will be most stable in a down configuration which effectively blocks proton transport from intra- to extracellular solution. Insight into the hydration of the proton channel is also provided—the transport of the excess proton dynamically hydrates the central region of the protein, which is a phenomenon observed for both this biomolecular system and in CcO.[36] This also replicates the finding of transient, dynamic water wires found in the CNT system.[33] Kinetic insights also provided rate constants for the proton transport process.

In the CcO system, MS-RMD simulations have characterized the free energy profile of proton transport through the D-channel, providing major insights into the mechanistic function of the enzyme.[36,37] The MS-RMD simulations obtain a clear mechanism and free-energy profile of proton transit, establishing key relationships between electron transfer reactions, the resulting electrostatic changes, and corresponding events in the proton transport chain. MS-RMD simulations were used with MetaD to establish the lowest energy pathway through the channel, and then the free energy profile was computed with umbrella sampling. Additional work[37] on a number of mutant structures showed how proton transport through the channel may be impaired, and then described the key gating mechanisms present in the channel. The latter study made use of extensive 2D-US, which tracked both the position of the proton CEC and the hydration around a key residue. The 2D PMFs reveal key barriers for proton transit and detailed insight into the decoupling mechanisms of different CcO mutants.[37]

Further research has considered a synthetic, minimally designed channel protein to demonstrate how water wire connectivity mediates proton transport.[115] This study aimed to explain the effect of dry, apolar patches in the proton conduction pathways. Using MS-RMD simulations, it was again shown that transient water wires are formed to connect dry regions in confined spaces, and that the formation of these wires is heavily influenced by the presence of the excess proton. To correctly track the transit of the proton through the pore, two CVs were required: a CEC-based CV, which tracks the location of the charge defect along the pore, and second, the water wire connectivity parameter,[86] which is closely related to the excess proton's water wire structure. Both CV's needed to be modeled simultaneously with two-dimensional umbrella sampling to ensure that the hydration and proton transport behavior is correctly considered.[86,115] In comparison to MS-RMD simulations, classical MD simulations of the same system were unable to fully characterize the extent of the water wire formation in the channel.[115]

In the realm of materials systems, MS-RMD has also proven valuable in obtaining mechanistic insight into excess proton behavior. In particular, the Nafion charge transport membrane has been studied in detail with MS-RMD simulations.[38−44,100,102] Nafion is a PFSA membrane polymer that is used in electrolyte membrane fuel cells to facilitate proton transport. A strong, molecular-level understanding of the mechanism and diffusion rate of protons through the PFSA membrane was obtained via extensive MS-RMD simulations using the SCI-MS-EVB algorithm. These simulations determined accurate diffusion rates and transport pathways through the membrane. Critically, it was found that proton hopping is critical to the transport of protons through the membrane, and that the sulfonate groups of the membrane help stabilize the proton in a more Zundel-like ($H_5O_2^+$) configuration. However, as the water concentration increases, the bulk Eigen-like ($H_9O_4^+$) solvation structure is preferred. Later work explored the effect of the chosen water model on the observed self-diffusion of the excess protons and compared the structural properties and proton transport of Nafion against another PFSA membrane from 3M.[40]

In summary, all of these examples described here reflect cases where proton shuttling over large distances and on long time scales proves crucial to understanding the fundamental structure and function of the system. The RAPTOR software has provided the vehicle to enable such simulations.

4. CONCLUDING REMARKS

MS-RMD occupies a critical junction in the simulation of processes where chemical reactivity and charge transport play a key role in the structure, dynamics, and function of the system.

In the case of proton transport, the ability of RAPTOR to dynamically treat Grotthuss proton shuttling and charge delocalization without explicitly computing the electronic structure is essential to accurately describe the charge transport behavior at low computational cost. The method's success in modeling complex charge transport processes with numerical accuracy and favorable comparison to both *ab initio* methods and experimental results highlights the strength and flexibility of multiscale reactive MD modeling approaches, where one coarse-grains key attributes from higher-level calculations onto a potential that may be evaluated rapidly enough to access the relevant length and times scales. The development of CVs that can accurately account for behavior mediated by charge transport phenomena—most importantly for proton transport, water wire formation—has further bolstered MS-RMD's potential. Future directions for the RAPTOR software package for MS-RMD will focus on further improvements to the computational performance (with a particular focus on GPU acceleration), better support for more flexible off-diagonal force field terms that will *enable the consideration of more complex chemical reactions*, and integration of the package with other MD engines for flexibility and potentially further performance improvements.

In particular, we hope to soon support neural network-based off-diagonal terms, where neural network inferences can be made to compute the off-diagonal forces and energies at each time step. Neural networks reflect a highly flexible functional form that is trained directly on *ab initio* data, and thus fit clearly into the MS-RMD paradigm. The proliferation of physics-constrained neural network models in recent years and recent work in the EVB framework that uses such neural networks lend credence to the approach for applications in proton transport and complex biomolecular reactions.[46,116] By fitting neural networks for just the off-diagonal components of the reaction, and fitting separate networks to separate matrix elements when appropriate, we hope to improve the stability and accuracy of the resulting model and avoid the criticism of neural network approaches as being "black-box". Neural network enhancements to MS-RMD will also open the door to the consideration of more complex chemical reactions, and more clearly and directly link MS-RMD to higher-level electronic structure calculations.

Additional improvements to RAPTOR's computational performance will focus on more efficiently leveraging GPU acceleration and further improvements to the speed and scalability of the *k*-space calculations. The current implementation of GPU acceleration for RAPTOR fails to fully saturate the GPU, and significant efficiency is thus lost as communication costs increase. Efficiency gains may be achieved by considering a multiple program (MP) approach for the GPUs, where communication costs will be reduced by assigning a single GPU to compute the *k*-space interactions. Increasing GPU utilization by better overlapping communication costs related to the FFTs will dramatically increase simulation speeds and allow for MS-RMD simulations to enjoy some of the benefits that classical MD has enjoyed from GPU acceleration over the past 10 years.

Another long-term goal for RAPTOR is to generalize its interface and enable coupling to other MD drivers, in order to take advantage of features that are available in other MD engines and to make MS-RMD simulations available for MD codes beyond LAMMPS. This will involve rewriting the RAPTOR-specific code pieces (state search, matrix diagonal-ization) as an independent, standalone library with a sufficiently flexible API that it can couple into various MD engines to conduct MD-specific operations (force and energy evaluation, integration) with the algorithms and features offered by that specific MD code.

■ ASSOCIATED CONTENT

ⓈI Supporting Information

The Supporting Information is available free of charge at https://pubs.acs.org/doi/10.1021/acs.jpcb.4c01987.

> Installation instructions for RAPTOR, instructions for raptoranalysis use, detailed timings for RAPTOR CPU benchmarks, and additional information on CGIS off-diagonal errors (PDF)

■ AUTHOR INFORMATION

Corresponding Author

Gregory A. Voth − *Department of Chemistry, Chicago Center for Theoretical Chemistry, James Franck Institute, and Institute for Biophysical Dynamics, The University of Chicago, Chicago, Illinois 60637, United States;* ⓞ orcid.org/0000-0002-3267-6748; Email: gavoth@uchicago.edu

Authors

Scott Kaiser − *Department of Chemistry, Chicago Center for Theoretical Chemistry, James Franck Institute, and Institute for Biophysical Dynamics, The University of Chicago, Chicago, Illinois 60637, United States;* ⓞ orcid.org/0009-0009-7183-5754

Zhi Yue − *Department of Chemistry, Chicago Center for Theoretical Chemistry, James Franck Institute, and Institute for Biophysical Dynamics, The University of Chicago, Chicago, Illinois 60637, United States;* ⓞ orcid.org/0000-0002-4231-7474

Yuxing Peng − *NVIDIA Corporation, Santa Clara, California 95051, United States*

Trung Dac Nguyen − *Research Computing Center, The University of Chicago, Chicago, Illinois 60637, United States*

Sijia Chen − *Department of Chemistry, Chicago Center for Theoretical Chemistry, James Franck Institute, and Institute for Biophysical Dynamics, The University of Chicago, Chicago, Illinois 60637, United States;* ⓞ orcid.org/0000-0003-2060-4920

Da Teng − *Department of Chemistry, Chicago Center for Theoretical Chemistry, James Franck Institute, and Institute for Biophysical Dynamics, The University of Chicago, Chicago, Illinois 60637, United States;* ⓞ orcid.org/0009-0000-1905-4277

Complete contact information is available at:
https://pubs.acs.org/10.1021/acs.jpcb.4c01987

Author Contributions

The manuscript was written through contributions of all authors.

Notes

The authors declare no competing financial interest.

■ ABBREVIATIONS

MS-RMD, multiscale reactive molecular dynamics; RAPTOR, Rapid Approach for Proton Transport and Other Reactions; CV, collective variable; QM/MM, quantum mechanics/molecular mechanics; ML, machine learning; NN, neural network; EVB, empirical valence bond; MS-EVB, multistate empirical valence bond; P^3M, particle−particle−particle mesh; SCI-MS-EVB, self-consistent iterative MS-EVB; MP, multiple program; CGIS, coarse-graining in interaction space; RDF, radial distribution function; MPI, message passing interface; SPMD, single program multiple data; GPGPU, general-purpose graphics processing unit; MSD, mean squared displacement; CEC, center of excess charge; WT-MetaD, well-tempered metadynamics; TT-MetaD, transition-tempered metadynamics; 2D-US, two-dimensional umbrella sampling; WHAM, weighted histogram analysis method; dTRAM, discrete transition-reweighted analysis method; CNT, carbon nanotube; PFSA, perfluorosulfonic acid; SNase, staphylococcal nuclease; AM2, influenza A M2 proton channel; CcO, cytochrome c oxidase

■ REFERENCES

(1) Senn, H. M.; Thiel, W. QM/MM Methods for Biomolecular Systems. *Angew. Chem., Int. Ed.* **2009**, *48* (7), 1198−1229.

(2) Carloni, P.; Rothlisberger, U.; Parrinello, M. The Role and Perspective of Ab Initio Molecular Dynamics in the Study of Biological Systems. *Acc. Chem. Res.* **2002**, *35* (6), 455−464.

(3) Tuckerman, M. E. Ab initio molecular dynamics: basic concepts, current trends and novel applications. *J. Phys.: condens. Matter.* **2002**, *14* (50), R1297.

(4) Hollingsworth, S. A.; Dror, R. O. Molecular Dynamics Simulation for All. *Neuron* **2018**, *99* (6), 1129−1143.

(5) Warshel, A.; Levitt, M. Theoretical Studies of Enzymic Reactions: Dielectric, Electrostatic and Steric Stabilization of the Carbonium In in the Reaction of Lsozyme. *J. Mol. Biol.* **1976**, *103* (2), 227−249.

(6) Lee, H.-S.; Tuckerman, M. E. Dynamical properties of liquid water from *ab initio* molecular dynamics performed in the complete basis set limit. *J. Chem. Phys.* **2007**, *126* (16), 164501.

(7) Calio, P. B.; Li, C.; Voth, G. A. Resolving the Structural Debate for the Hydrated Excess Proton in Water. *J. Am. Chem. Soc.* **2021**, *143* (44), 18672−18683.

(8) Poltavsky, I.; Tkatchenko, A. Machine Learning Force Fields: Recent Advances and Remaining Challenges. *J. Phys. Chem. Lett.* **2021**, *12* (28), 6551−6564.

(9) Unke, O. T.; Chmiela, S.; Sauceda, H. E.; Gastegger, M.; Poltavsky, I.; Schütt, K. T.; Tkatchenko, A.; Müller, K.-R.-R. Machine Learning Force Fields. *Chem. Rev.* **2021**, *121* (16), 10142−10186.

(10) de Grotthuss, C. J. T. Sur la décomposition de l'eau et des corps qu'elle tient en dissolution à l'aide de l'électricité galvanique. *Ann. Chim.* **1806**, *58*, 54−74.

(11) Cukierman, S. E. T. Grotthuss! and other unfinished stories. *Biochim. Biophys. Acta* **2006**, *1757* (8), 876−885.

(12) Watkins, L. C.; Liang, R.; Swanson, J. M. J.; DeGrado, W. F.; Voth, G. A. Proton-Induced Conformational and Hydration Dynamics in the Influenza A M2 Channel. *J. Am. Chem. Soc.* **2019**, *141* (29), 11667−11676.

(13) Peng, Y.; Swanson, J. M. J.; Kang, S.-G.; Zhou, R.; Voth, G. A. Hydrated Excess Protons Can Create Their Own Water Wires. *J. Phys. Chem. B* **2015**, *119* (29), 9212−9218.

(14) Warshel, A.; Weiss, R. M. An Empirical Valence Bond Approach for Comparing Reactions in Solutions and in Enzymes. *J. Am. Chem. Soc.* **1980**, *102* (20), 6218−6226.

(15) Kamerlin, S. C. L.; Warshel, A. The empirical valence bond model: theory and applications. *WIREs Comput. Mol. Sci.* **2011**, *1* (1), 30−45.

(16) Schmitt, U. W.; Voth, G. A. Multistate Empirical Valence Bond Model for Proton Transport in Water. *J. Phys. Chem. B* **1998**, *102* (29), 5547−5551.

(17) Schmitt, U. W.; Voth, G. A. The computer simulation of proton transport in water. *J. Chem. Phys.* **1999**, *111* (20), 9361−9381.

(18) Vuilleumier, R.; Borgis, D. Quantum Dynamics of an Excess Proton in Water Using an Extended Empirical Valence-Bond Hamiltonian. *J. Phys. Chem. B* **1998**, *102* (22), 4261−4264.

(19) Vuilleumier, R.; Borgis, D. Transport and spectroscopy of the hydrated proton: A molecular dynamics study. *J. Chem. Phys.* **1999**, *111* (9), 4251−4266.

(20) Lobaugh, J.; Voth, G. A. The quantum dynamics of an excess proton in water. *J. Chem. Phys.* **1996**, *104* (5), 2056−2069.

(21) Čuma, M.; Schmitt, U. W.; Voth, G. A. A Multi-State Empirical Valence Bond Model for Weak Acid Dissociation in Aqueous Solution. *J. Phys. Chem. A* **2001**, *105* (12), 2814−2823.

(22) Day, T. J. F.; Soudackov, A. V.; Čuma, M.; Schmitt, U. W.; Voth, G. A. A second generation multistate empirical valence bond model for proton transport in aqueous systems. *J. Chem. Phys.* **2002**, *117* (12), 5839−5849.

(23) Wu, Y.; Chen, H.; Wang, F.; Paesani, F.; Voth, G. A. An Improved Multistate Empirical Valence Bond Model for Aqueous Proton Solvation and Transport. *J. Phys. Chem. B* **2008**, *112* (2), 467−482.

(24) Nelson, J. G.; Peng, Y.; Silverstein, D. W.; Swanson, J. M. J. Multiscale Reactive Molecular Dynamics for Absolute pK_a Predictions and Amino Acid Deprotonation. *J. Chem. Theory Comput.* **2014**, *10* (7), 2729−2737.

(25) Biswas, R.; Tse, Y.-L. S.; Tokmakoff, A.; Voth, G. A. Role of Presolvation and Anharmonicity in Aqueous Phase Hydrated Proton Solvation and Transport. *J. Phys. Chem. B* **2016**, *120* (8), 1793−1804.

(26) Knight, C.; Maupin, C. M.; Izvekov, S.; Voth, G. A. Defining Condensed Phase Reactive Force Fields from ab Initio Molecular Dynamics Simulations: The Case of the Hydrated Excess Proton. *J. Chem. Theory Comput.* **2010**, *6* (10), 3223−3232.

(27) Knight, C.; Lindberg, G. E.; Voth, G. A. Multiscale reactive molecular dynamics. *J. Chem. Phys.* **2012**, *137* (22), 22A525.

(28) Knight, C.; Voth, G. A. The Curious Case of the Hydrated Proton. *Acc. Chem. Res.* **2012**, *45* (1), 101−109.

(29) Tse, Y.-L. S.; Chen, C.; Lindberg, G. E.; Kumar, R.; Voth, G. A. Propensity of Hydrated Excess Protons and Hydroxide Anions for the Air−Water Interface. *J. Am. Chem. Soc.* **2015**, *137* (39), 12610−12616.

(30) Kumar, R.; Knight, C.; Voth, G. A. Exploring the behaviour of the hydrated excess proton at hydrophobic interfaces. *Faraday Discuss.* **2014**, *167*, 263−278.

(31) Iuchi, S.; Chen, H.; Paesani, F.; Voth, G. A. Hydrated Excess Proton at Water-Hydrophobic Interfaces. *J. Phys. Chem. B* **2009**, *113* (13), 4017−4030.

(32) Lee, S.; Mayes, H. B.; Swanson, J. M. J.; Voth, G. A. The Origin of Coupled Chloride and Proton Transport in a Cl$^-$/H$^+$ Antiporter. *J. Am. Chem. Soc.* **2016**, *138* (45), 14923−14930.

(33) Lee, S.; Swanson, J. M. J.; Voth, G. A. Multiscale Simulations Reveal Key Aspects of the Proton Transport Mechanism in the ClC-ec1 Antiporter. *Biophys. J.* **2016**, *110* (6), 1334−1345.

(34) Li, C.; Voth, G. A. Accurate and Transferable Reactive Molecular Dynamics Models from Constrained Density Functional Theory. *J. Phys. Chem. B* **2021**, *125* (37), 10471−10480.

(35) Liang, R.; Li, H.; Swanson, J. M. J.; Voth, G. A. Multiscale simulation reveals a multifaceted mechanism of proton permeation

through the influenza A M2 proton channel. *Proc. Natl. Acad. Sci. U. S. A.* **2014**, *111* (26), 9396−9401.

(36) Liang, R.; Swanson, J. M. J.; Peng, Y.; Wikström, M.; Voth, G. A. Multiscale simulations reveal key features of the proton-pumping mechanism in cytochrome *c* oxidase. *Proc. Natl. Acad. Sci. U. S. A.* **2016**, *113* (27), 7420−7425.

(37) Liang, R.; Swanson, J. M. J.; Wikström, M.; Voth, G. A. Understanding the essential proton-pumping kinetic gates and decoupling mutations in cytochrome *c* oxidase. *Proc. Natl. Acad. Sci. U. S. A.* **2017**, *114* (23), 5924−5929.

(38) Feng, S.; Savage, J.; Voth, G. A. Effects of Polymer Morphology on Proton Solvation and Transport in Proton-Exchange Membranes. *J. Phys. Chem. C* **2012**, *116* (36), 19104−19116.

(39) Jorn, R.; Voth, G. A. Mesoscale Simulation of Proton Transport in Proton Exchange Membranes. *J. Phys. Chem. C* **2012**, *116* (19), 10476−10489.

(40) Tse, Y.-L. S.; Herring, A. M.; Kim, K.; Voth, G. A. Molecular Dynamics Simulations of Proton Transport in 3M and Nafion Perfluorosulfonic Acid Membranes. *J. Phys. Chem. C* **2013**, *117* (16), 8079−8091.

(41) Liu, S.; Savage, J.; Voth, G. A. Mesoscale Study of Proton Transport in Proton Exchange Membranes: Role of Morphology. *J. Phys. Chem. C* **2015**, *119* (4), 1753−1762.

(42) Savage, J.; Voth, G. A. Proton Solvation and Transport in Realistic Proton Exchange Membrane Morphologies. *J. Phys. Chem. C* **2016**, *120* (6), 3176−3186.

(43) Arntsen, C.; Savage, J.; Tse, Y.-L. S.; Voth, G. A. Simulation of Proton Transport in Proton Exchange Membranes with Reactive Molecular Dynamics. *Fuel Cells* **2016**, *16* (6), 695−703.

(44) Chen, C.; Tse, Y. L.; Lindberg, G. E.; Knight, C.; Voth, G. A. Hydroxide Solvation and Transport in Anion Exchange Membranes. *J. Am. Chem. Soc.* **2016**, *138* (3), 991−1000.

(45) Yamashita, T.; Peng, Y.; Knight, C.; Voth, G. A. Computationally Efficient Multiconfigurational Reactive Molecular Dynamics. *J. Chem. Theory Comput.* **2012**, *8* (12), 4863−4875.

(46) Stoppelman, J. P.; McDaniel, J. G. Physics-based, neural network force fields for reactive molecular dynamics: Investigation of carbene formation from [EMIM$^+$][OAc$^-$]. *J. Chem. Phys.* **2021**, *155* (10), 104112.

(47) Lee, S.; Liang, R.; Voth, G. A.; Swanson, J. M. J. Computationally Efficient Multiscale Reactive Molecular Dynamics to Describe Amino Acid Deprotonation in Proteins. *J. Chem. Theory Comput.* **2016**, *12* (2), 879−891.

(48) Plimpton, S. Fast Parallel Algorithms for Short-Range Molecular Dynamics. *J. Comput. Phys.* **1995**, *117* (1), 1−19.

(49) Thompson, A. P.; Aktulga, H. M.; Berger, R.; Bolintineanu, D. S.; Brown, W. M.; Crozier, P. S.; in't Veld, P. J.; Kohlmeyer, A.; Moore, S. G.; Nguyen, T. D.; et al. LAMMPS - a flexible simulation tool for particle-based materials modeling at the atomic, meso, and continuum scales. *Comput. Phys. Commun.* **2022**, *271*, 108171.

(50) Sandia National Laboratories. *LAMMPS Molecular Dynamics Simulator*, Sandia National Laboratories: https://lammps.sandia.gov.

(51) Laio, A.; Parrinello, M. Escaping free-energy minima. *Proc. Natl. Acad. Sci. U. S. A.* **2002**, *99* (20), 12562−12566.

(52) Barducci, A.; Bussi, G.; Parrinello, M. Well-Tempered Metadynamics: A Smoothly Converging and Tunable Free-Energy Method. *Phys. Rev. Lett.* **2008**, *100* (2), 020603.

(53) Dama, J. F.; Rotskoff, G.; Parrinello, M.; Voth, G. A. Transition-Tempered Metadynamics: Robust, Convergent Metadynamics via On-the-Fly Transition Barrier Estimation. *J. Chem. Theory Comput.* **2014**, *10* (9), 3626−3633.

(54) Bussi, G.; Laio, A. Using metadynamics to explore complex free-energy landscapes. *Nat. Rev. Phys.* **2020**, *2* (4), 200−212.

(55) Dama, J. F.; Parrinello, M.; Voth, G. A. Well-tempered metadynamics converges asymptotically. *Phys. Rev. Lett.* **2014**, *112* (24), 240602.

(56) Torrie, G. M.; Valleau, J. P. Nonphysical Sampling Distributions in Monte Carlo Free-Energy Estimation: Umbrella Sampling. *J. Comput. Phys.* **1977**, *23* (2), 187−199.

(57) Kästner, J. Umbrella sampling. *WIREs Comput. Mol. Sci.* **2011**, *1* (6), 932−942.

(58) Sugita, Y.; Okamoto, Y. Replica-exchange molecular dynamics method for protein folding. *Chem. Phys. Lett.* **1999**, *314* (1−2), 141−151.

(59) Sugita, Y.; Kitao, A.; Okamoto, Y. Multidimensional replica-exchange method for free-energy calculations. *J. Chem. Phys.* **2000**, *113* (15), 6042−6051.

(60) Wu, Y.; Tepper, H. L.; Voth, G. A. Flexible simple point-charge water model with improved liquid-state properties. *J. Chem. Phys.* **2006**, *124* (2), 024503.

(61) Zuchniarz, J.; Liu, Y.; Li, C.; Voth, G. A. Accurate pK_a Calculations in Proteins with Reactive Molecular Dynamics Provide Physical Insight Into the Electrostatic Origins of Their Values. *J. Phys. Chem. B* **2022**, *126* (38), 7321−7330.

(62) MacKerell, A. D., Jr; Bashford, D.; Bellott, M.; Dunbrack, R. L., Jr; Evanseck, J. D.; Field, M. J.; Fischer, S.; Gao, J.; Guo, H.; Ha, S.; Joseph-McCarthy, D.; Kuchnir, L.; Kuczera, K.; Lau, F. T.; Mattos, C.; Michnick, S.; Ngo, T.; Nguyen, D. T.; Prodhom, B.; Reiher, W. E.; Roux, B.; Schlenkrich, M.; Smith, J. C.; Stote, R.; Straub, J.; Watanabe, M.; Wiórkiewicz-Kuczera, J.; Yin, D.; Karplus, M. All-Atom Empirical Potential for Molecular Modeling and Dynamics Studies of Proteins. *J. Phys. Chem. B* **1998**, *102* (18), 3586−3616.

(63) MacKerell, A. D., Jr; Feig, M.; Brooks, C. L. Improved Treatment of the Protein Backbone in Empirical Force Fields. *J. Am. Chem. Soc.* **2004**, *126* (3), 698−699.

(64) Mackerell, A. D., Jr; Feig, M.; Brooks, I. C. L. Extending the Treatment of Backbone Energetics in Protein Force Fields: Limitations of Gas-Phase Quantum Mechanics in Reproducing Protein Conformational Distributions in Molecular Dynamics Simulations. *J. Comput. Chem.* **2004**, *25* (11), 1400−1415.

(65) Best, R. B.; Zhu, X.; Shim, J.; Lopes, P. E. M.; Mittal, J.; Feig, M.; MacKerell, A. D., Jr Optimization of the Additive CHARMM All-Atom Protein Force Field Targeting Improved Sampling of the Backbone ϕ, ψ and Side-Chain χ 1 and χ 2 Dihedral Angles. *J. Chem. Theory Comput.* **2012**, *8* (9), 3257−3273.

(66) Huang, J.; Rauscher, S.; Nawrocki, G.; Ran, T.; Feig, M.; de Groot, B. L.; Grubmüller, H.; MacKerell, J. A. D. CHARMM36m: An improved force field for folded and intrinsically disordered proteins. *Nat. Methods* **2017**, *14* (1), 71−73.

(67) Stoppelman, J. P.; McDaniel, J. G. N−Heterocyclic Carbene Formation in the Ionic Liquid [EMIM$^+$][OAc$^-$]: Elucidating Solvation Effects with Reactive Molecular Dynamics Simulations. *J. Phys. Chem. B* **2023**, *127* (23), 5317−5333.

(68) Hockney, R. W.; Eastwood, J. W.Particle-Particle−Particle-Mesh (P^{3}M) Algorithm. In *Computer Simulation Using Particles*, 1 st ed; Hockney, R. W.; Eastwood, J. W., Eds.; McGraw-Hill International Book Co.: New York, NY, USA, 1981; pp. 267304.

(69) Pollock, E. L.; Glosli, J. Comments on P^{3}M, FMM, and the Ewald method for large periodic Coulombic systems. *Comput. Phys. Commun.* **1996**, *95* (2−3), 93−110.

(70) Accardi, A.; Miller, C. Secondary active transport mediated by a prokaryotic homologue of ClC Cl$^-$ channels. *Nature* **2004**, *427* (6977), 803−807.

(71) Wang, F.; Voth, G. A. A linear-scaling self-consistent generalization of the multistate empirical valence bond method for multiple excess protons in aqueous systems. *J. Chem. Phys.* **2005**, *122* (14), 144105.

(72) Izvekov, S.; Swanson, J. M. J.; Voth, G. A. Coarse-Graining in Interaction Space: A Systematic Approach for Replacing Long-Range Electrostatics with Short-Range Potentials. *J. Phys. Chem. B* **2008**, *112* (15), 4711−4724.

(73) Lange, A. W.; Nelson, G.; Knight, C.; Voth, G. A. Multiscale Molecular Simulations at the Petascale (Parallelization of Reactive Force Model for Blue Gene/Q). In *ALCF-2 Early Science Program Technical Report*; Argonne National Laboratory: Argonne, IL, USA, 2013.

(74) Peng, Y.; Knight, C.; Blood, P.; Crosby, L.; Voth, G. A. Extending Parallel Scalability of LAMMPS and Multiscale Reactive

Molecular Simulations. In *XSEDE'12: proceedings of the 1st Conference of the Extreme Science and Engineering Discovery Environment: bridging from the eXtreme to the campus and beyond*; Association for Computing Machinery: Chicago, IL, USA, 2012.

(75) Hess, B.; Kutzner, C.; Lindahl, E. GROMACS 4: Algorithms for Highly Efficient, Load-Balanced, and Scalable Molecular Simulation. *J. Chem. Theory Comput.* **2008**, *4* (3), 435−447.

(76) Brown, W. M.; Wang, P.; Plimpton, S. J.; Tharrington, A. N. Implementing molecular dynamics on hybrid high performance computers − short range forces. *Comput. Phys. Commun.* **2011**, *182* (4), 898−911.

(77) Brown, W. M.; Kohlmeyer, A.; Plimpton, S. J.; Tharrington, A. N. Implementing molecular dynamics on hybrid high performance computers − Particle−particle particle-mesh. *Comput. Phys. Commun.* **2012**, *183* (3), 449−459.

(78) Brown, W. M.; Yamada, M. Implementing molecular dynamics on hybrid high performance computers—Three-body potentials. *Comput. Phys. Commun.* **2013**, *184* (12), 2785−2793.

(79) Nguyen, T. D. GPU-accelerated Tersoff potentials for massively parallel Molecular Dynamics simulations. *Comput. Phys. Commun.* **2017**, *212*, 113−122.

(80) Feller, S. E.; MacKerell, A. D. An improved empirical potential energy function for molecular simulations of phospholipids. *J. Phys. Chem. B* **2000**, *104* (31), 7510−7515.

(81) Klauda, J. B.; Brooks, B. R.; MacKerell, A. D.; Venable, R. M.; Pastor, R. W. An ab Initio Study on the Torsional Surface of Alkanes and Its Effect on Molecular Simulations of Alkanes and a DPPC Bilayer. *J. Phys. Chem. B* **2005**, *109* (11), 5300−5311.

(82) Martyna, G. J.; Klein, M. L.; Tuckerman, M. Nosé−Hoover chains: The canonical ensemble via continuous dynamics. *J. Chem. Phys.* **1992**, *97* (4), 2635−2643.

(83) The PLUMED consortium Promoting transparency and reproducibility in enhanced molecular simulations. *Nat. Methods* **2019**, *16* (8), 670673.

(84) Tribello, G. A.; Bonomi, M.; Branduardi, D.; Camilloni, C.; Bussi, G. PLUMED 2: New feathers for an old bird. *Comput. Phys. Commun.* **2014**, *185* (2), 604−613.

(85) Maupin, C. M.; Wong, K. F.; Soudackov, A. V.; Kim, S.; Voth, G. A. A Multistate Empirical Valence Bond Description of Protonatable Amino Acids. *J. Phys. Chem. A* **2006**, *110* (2), 631−639.

(86) Li, C.; Voth, G. A. A quantitative paradigm for water-assisted proton transport through proteins and other confined spaces. *Proc. Natl. Acad. Sci. U. S. A.* **2021**, *118* (49), No. e2113141118.

(87) Li, C.; Yue, Z.; Espinoza-Fonseca, L. M.; Voth, G. A. Multiscale Simulation Reveals Passive Proton Transport Through SERCA on the Microsecond Timescale. *Biophys. J.* **2020**, *119* (5), 1033−1040.

(88) Hénin, J. R. M.; Lelièvre, T.; Shirts, M. R.; Valsson, O.; Delemotte, L. Enhanced Sampling Methods for Molecular Dynamics Simulations. *Living J. Comput. Mol. Sci.* **2022**, *4* (1), 1583.

(89) Kumar, S.; Rosenberg, J. M.; Bouzida, D.; Swendsen, R. H.; Kollman, P. A. The Weighted Histogram Analysis Method for Free-Energy Calculations on Biomolecules. I. The Method. *J. Comput. Chem.* **1992**, *13* (8), 1011−1021.

(90) Souaille, M.; Roux, B. Extension to the weighted histogram analysis method: combining umbrella sampling with free energy calculations. *Comput. Phys. Commun.* **2001**, *135* (1), 40−57.

(91) Wu, H.; Mey, A. S. J. S.; Rosta, E.; Noé, F. Statistically optimal analysis of state-discretized trajectory data from multiple thermodynamic states. *J. Chem. Phys.* **2014**, *141* (21), 214106.

(92) Scherer, M. K.; Trendelkamp-Schroer, B.; Paul, F.; Pérez-Hernández, G.; Hoffmann, M.; Plattner, N.; Wehmeyer, C.; Prinz, J.-H.; Noé, F. PyEMMA 2: A Software Package for Estimation, Validation, and Analysis of Markov Models. *J. Chem. Theory Comput.* **2015**, *11* (11), 5525−5542.

(93) Weinan, E.; Ren, W.; Vanden-Eijnden, E. Simplified and improved string method for computing the minimum energy paths in barrier-crossing events. *J. Chem. Phys.* **2007**, *126* (16), 164103.

(94) Liu, Y.; Li, C.; Voth, G. A. Generalized Transition State Theory Treatment of Water-Assisted Proton Transport Processes in Proteins. *J. Phys. Chem. B* **2022**, *126* (49), 10452−10459.

(95) Markovitch, O.; Chen, H.; Izvekov, S.; Paesani, F.; Voth, G. A.; Agmon, N. Special Pair Dance and Partner Selection: Elementary Steps in Proton Transport in Liquid Water. *J. Phys. Chem. B* **2008**, *112* (31), 9456−9466.

(96) Petersen, M. K.; Iyengar, S. S.; Day, T. J. F.; Voth, G. A. The Hydrated Proton at the Water Liquid/Vapor Interface. *J. Phys. Chem. B* **2004**, *108* (39), 14804−14806.

(97) Li, Z.; Li, C.; Wang, Z.; Voth, G. A. What Coordinate Best Describes the Affinity of the Hydrated Excess Proton for the Air−Water Interface? *J. Phys. Chem. B* **2020**, *124* (24), 5039−5046.

(98) Chen, S.; Li, Z.; Voth, G. A. Acidic Conditions Impact Hydrophobe Transfer across the Oil−Water Interface in Unusual Ways. *J. Phys. Chem. B* **2023**, *127* (17), 3911−3918.

(99) Ma, X.; Li, C.; Martinson, A. B. F.; Voth, G. A. Water-Assisted Proton Transport in Confined Nanochannels. *J. Phys. Chem. C* **2020**, *124* (29), 16186−16201.

(100) Feng, S.; Voth, G. A. Proton Solvation and Transport in Hydrated Nafion. *J. Phys. Chem. B* **2011**, *115* (19), 5903−5912.

(101) Petersen, M. K.; Voth, G. A. Characterization of the Solvation and Transport of the Hydrated Proton in the Perfluorosulfonic Acid Membrane Nafion. *J. Phys. Chem. B* **2006**, *110* (37), 18594−18600.

(102) Savage, J.; Voth, G. A. Persistent Subdiffusive Proton Transport in Perfluorosulfonic Acid Membranes. *J. Phys. Chem. Lett.* **2014**, *5* (17), 3037−3742.

(103) Savage, J.; Tse, Y. L. S.; Voth, G. A. Proton Transport Mechanism of Perfluorosulfonic Acid Membranes. *J. Phys. Chem. C* **2014**, *118* (31), 17436−17445.

(104) Teng, D.; Voth, G. A. Ligand binding by the small multidrug-resistant transporter EmrE. *Biophys. J.* **2023**, *122* (3), 400a.

(105) Liang, R.; Swanson, J. M. J.; Madsen, J. J.; Hong, M.; DeGrado, W. F.; Voth, G. A. Acid activation mechanism of the influenza A M2 proton channel. *Proc. Natl. Acad. Sci. U. S. A.* **2016**, *113* (45), No. E6955−E6964.

(106) Watkins, L. C.; DeGrado, W. F.; Voth, G. A. Influenza A M2 Inhibitor Binding Understood through Mechanisms of Excess Proton Stabilization and Channel Dynamics. *J. Am. Chem. Soc.* **2020**, *142* (41), 17425−17433.

(107) Watkins, L. C.; DeGrado, W. F.; Voth, G. A. Multiscale Simulation of an Influenza A M2 Channel Mutant Reveals Key Features of Its Markedly Different Proton Transport Behavior. *J. Am. Chem. Soc.* **2022**, *144* (2), 769−776.

(108) Das, S.; Imoto, S.; Sun, S.; Nagata, Y.; Backus, E. H. G.; Bonn, M. Nature of Excess Hydrated Proton at the Water−Air Interface. *J. Am. Chem. Soc.* **2020**, *142* (2), 945−952.

(109) Chiang, K.-Y.; Dalstein, L.; Wen, Y.-C. Affinity of Hydrated Protons at Intrinsic Water/Vapor Interface Revealed by Ion-Induced Water Alignment. *J. Phys. Chem. Lett.* **2020**, *11* (3), 696−701.

(110) Miller, C. ClC chloride channels viewed through a transporter lens. *Nature* **2006**, *440* (7083), 484−489.

(111) Capaldi, R. A. Structure and Function of Cytochrome *c* Oxidase. *Annu. Rev. Biochem.* **1990**, *59*, 569−596.

(112) Yoshikawa, S.; Shimada, A. Reaction Mechanism of Cytochrome *c* Oxidase. *Chem. Rev.* **2015**, *115* (4), 1936−1989.

(113) Pinto, L. H.; Lamb, R. A. The M2 proton channels of influenza A and B viruses. *J. Biol. Chem.* **2006**, *281* (14), 8997−9000.

(114) Pielak, R. M.; Chou, J. J. Influenza M2 proton channels. *Biochim. Biophys. Acta* **2011**, *1808* (2), 522−529.

(115) Kratochvil, H. T.; Watkins, L. C.; Mravic, M.; Thomaston, J. L.; Nicoludis, J. M.; Somberg, N. H.; Liu, L.; Hong, M.; Voth, G. A.; DeGrado, W. F. Transient water wires mediate selective proton transport in designed channel proteins. *Nat. Chem.* **2023**, *15* (7), 1012−1021.

(116) Schütt, K. T.; Sauceda, H. E.; Kindermans, P.-J.; Tkatchenko, A.; Müller, K.-R. SchNet − A deep learning architecture for molecules and materials. *J. Chem. Phys.* **2018**, *148* (24), 241722.